Cyprus University of Technology

HANGZHOU DIANZI UNIVERSITY

Master's Thesis

Research on MEMS Accelerometers Based on Silicon Nanowire Arrays

Yin Zhiyuan

Limassol, May 2025

MSc in Electronics Science and Technology

CYPRUS UNIVERSITY OF TECHNOLOGY

FACULTY OF ENGINEERING AND TECHNOLOGY

DEPARTMENT OF ELECTRICAL ENGINEERING AND COMPUTER ENGINEERING AND INFORMATICS

Master's Thesis

Research on MEMS Accelerometers Based on Silicon Nanowire Arrays

Yin Zhiyuan

Supervisor

Professor Kyriacos Kalli

Limassol, Month and year of thesis submission

Approval Form

Master's Thesis

Research on MEMS Accelerometers Based on Silicon Nanowire Arrays

Presented by

Yin Zhiyuan

Supervisor: [Kyriacos Kalli]

Member of the committee: [Paul Christodoulides]

Member of the committee: [Andreas Ioannou]

Cyprus University of Technology

Limassol, Month and year of thesis submission

Copyrights

The approval of the thesis by the Department of Electrical Engineering and Computer Engineering and Informatics does not necessarily imply the approval by the Department of the writer's views.

Acknowledgements

The completion of the current thesis could not have been accomplished without the guidance of my supervisor, Professor Kyriacos Kalli, Faculty of Engineering and Technology, Cyprus University of Technology. I would like to express him my sincere gratitude for giving me the opportunity to get involved in his research. His guidance and very constructive criticism have contributed immensely to the evolution of the current research.

I would also like to express a deep sense of gratitude to all the employees of laboratory (CUT) who provided amount of their precious time to taught me the technology to carry out the study and offered me their invaluable knowledge and support.

ABSTRACT

Silicon nanowires, as an emerging material with giant piezoresistive effects and high bandwidth characteristics, can significantly enhance the sensor's response to high-frequency dynamic vibrations compared to traditional piezoresistive materials. Leveraging this property, I designed a MEMS accelerometer based on a silicon nanowire array.

We began by conducting in-depth experiments on the giant piezoresistive effect of silicon nanowires to investigate their resistance variation under different stress conditions. During the structural design phase, we modelled the sensor using SOLIDWORKS and optimized the structure of the sensing elements through finite element analysis with COMSOL. Both static and dynamic simulations confirmed the rationality of the design.

Subsequently, a top-down fabrication method was employed to produce the silicon nanowire array. Finally, performance testing was carried out, revealing that the proposed silicon nanowire-based MEMS accelerometer achieved a single nanowire sensitivity of 0.44 Ω/g, a resistance of 16.25 MΩ, a bandwidth of 0–19.5 kHz, and a maximum operating acceleration of 115 g.

Keywords: MEMS; Silicon nanowires； accelerometer; giant piezoresistive effect; finite element analysis

Table of Contents

LIST OF TABLES

LIST OF FIGURES

LIST OF ABBREVIATIONS

CUT:	Cyprus University of Technology
MEMS:	Micro-Electro-Mechanical System
SOI:	Silicon-On-Insulator
RGT:	Resonant Gate Transistor
SIN:	Silicon Nitride
CVD:	Chemical Vapor Deposition
BOE:	Buffered Oxide Etch
SINW:	Silicon Nanowire

1 Introduction

1.1 State of the Art

The development of MEMS sensors can be divided into several important stages: firstly, in 1947, William Shockley, John Bardeen and Walter Brattain of Bell Labs succeeded in creating the first point contact transistor. This transistor utilised germanium, a semi-conducting chemical element. This invention demonstrated the ability to make transistors from semiconductor materials, allowing better control of voltage and current. It also opened the door to making smaller and smaller transistors. The germanium NPN growth junction transistor was patented by William Shockley in 1948. The first transistor was about half an inch tall, which was undoubtedly huge compared to today's standards. Today, scientists can create nanotransistors that are about 1 nanometre in diameter. For reference, a human hair is about 60-100 microns[1−2].

In 1954, Smith discovered the piezoresistive effect of semiconductor materials such as silicon and germanium. This piezoresistive effect in semiconductors can be orders of magnitude greater than in metals. This discovery was important for MEMS because it showed that silicon and germanium could sense the pressure of air or water better than metals. The discovery of the piezoresistive effect in semiconductors led to the commercial development of silicon strain gauges in 1958. In 1959, Kulite Corporation was founded as the first commercial source of bare silicon strain gauges[3]. As shown in Figure 1.1, a pressure sensor that utilises the piezoresistive effect of metals (MTTC pressure sensor).

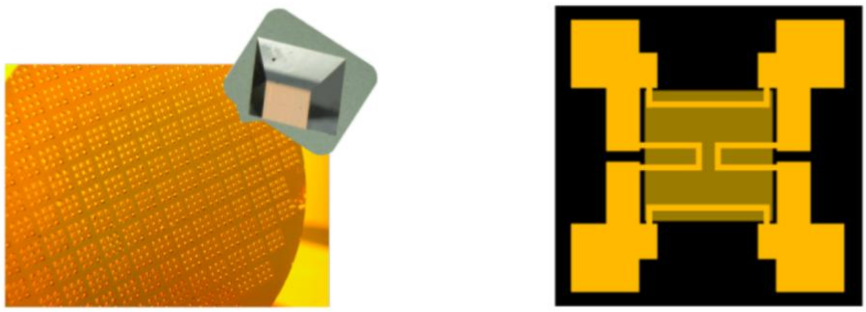

Figure 1.1 Seismic Sensor Schematic

When the transistor was invented, there was a limit to the actual size of each transistor because it had to be connected to wires and other electronic devices. As a result, the shrinking of the transistor came to a standstill until the advent of the ‘integrated circuit’. An integrated circuit would consist of transistors, resistors, capacitors, and wires to meet the needs of a particular application. If an integrated circuit could be made entirely on a single substrate, the entire device could be made smaller[4−6]. Almost at the same time, two people independently developed integrated circuits; in 1958, Jack Kilby, working for Texas Instruments, developed a working model of a ‘solid-state circuit’, which consisted of a transistor, three resistors and wires. This circuit consisted of a transistor, three resistors and a capacitor, all mounted on a sheet of germanium. Soon after, Robert Noyce of Fairchild Semiconductor made the first ‘unit circuit’. This integrated circuit was made on a silicon chip, and Robert Noyce received his first patent in 1961[7].

In 1964, a Westinghouse team led by Harvey Nathanson produced the first mass-produced MEMS device. This device, which connected mechanical and electronic components together, was called a resonant gate transistor (RGT) [8]. The RGT in Figure 1.2 differed from conventional transistors in that it was not fixed to the gate oxide. Instead, it is movable and cantilevered with respect to the substrate. Electrostatic attraction controls the distance between the gate and the substrate.The RGT is the earliest example of a microelectrostatic actuator. It was also the first demonstration of surface micromachining technology.

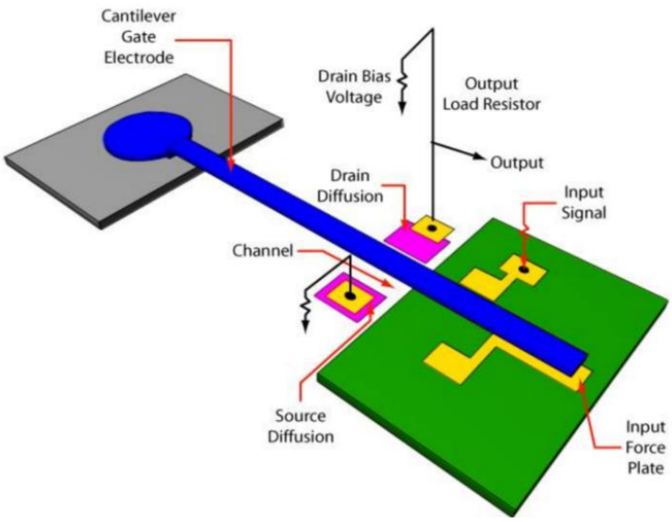

Figure 1.2 Resonant Gate Transistor

The fabrication of silicon transistors in the early 1960s brought about an isotropic etching process for silicon. Isotropic etching uses a chemical process to remove material from a substrate. Since the etching rate is uniform in all directions, the material is removed equally in all directions. In the late 1960s and early 1970s, Waggener published a paper entitled ‘Electrochemically Controlled Thinning of Silicon’, which illustrated anisotropic wet etching of silicon. Silicon can be selectively etched away by either method to form a variety of structures including V-grooves, pyramidal lattices, and microcavities. Electrochemical anisotropic etching is very important in microsystems fabrication because it is the basis for bulk micromachining processes. Bulk micromachining etches away a relatively large portion of the silicon substrate, leaving behind the desired structure. Since its inception, bulk micromachining has been a very powerful method for fabricating micromechanical components such as microfluidic channels, nozzles, diaphragms, suspension beams, and other moving or structural components[9−10].

In the 1970s, Kurt Peterson of IBM Research Laboratories developed a micromechanical pressure sensor using silicon diaphragms[11]. The thin film sheet allowed for greater deformation and therefore higher sensitivity than other diaphragm pressure sensors available at the time. This thin diaphragm pressure sensor was used in a large number of blood pressure monitoring devices and was arguably one of the earliest commercial successes of microsystem devices.

In the early 1980s, a team at the Nuclear Research Centre in Karlsruhe, Germany, developed a new process called LIGA, which is the German acronym for X-ray Lithographie (X-ray Lithography), Galvanoformung (Electroplating) and Abformung (Forming). This process is very important in microsystems manufacturing because it allows the fabrication of high aspect ratio microstructures. High aspect ratio structures are very thin, or narrow and tall structures, such as channels.LIGA can achieve ratios of up to 100:1, and LIGA structures have precise dimensions and low surface roughness[12]. Into the 1980s, MEMS technology was gradually made practical, in particular, Analog Devices introduced the world's first commercial micromechanical accelerometer, ADXL100, which provided revolutionary technical support for automotive airbags and other fields. During this period, MEMS devices began to make their mark in the industrial and consumer markets.

By the 1990s, as lithography and microfabrication processes matured, MEMS sensors were significantly improved and entered mass production.In 1992, Cornell University developed a batch microfabrication process called Single Crystal Reactive Etching and Metallisation (SCREAM) in Figure 1.3. It was developed to create released microstructures from single-crystal silicon and single-crystal gallium arsenide (GaAs.) In 1993, Analog Devices was the first to mass-produce surface-micromachined accelerometers. Previously, in the 1980s, TRW produced a sensor that sold for about $20 each. And the automotive industry used Analog Devices' accelerometers in airbags, which sold for about $5 each. This reduced the cost of airbag electronics by about 75 per cent[13−17]. The Analog Devices accelerometer was highly reliable, small and inexpensive. Its record-breaking sales increased the use of airbags in automobiles.

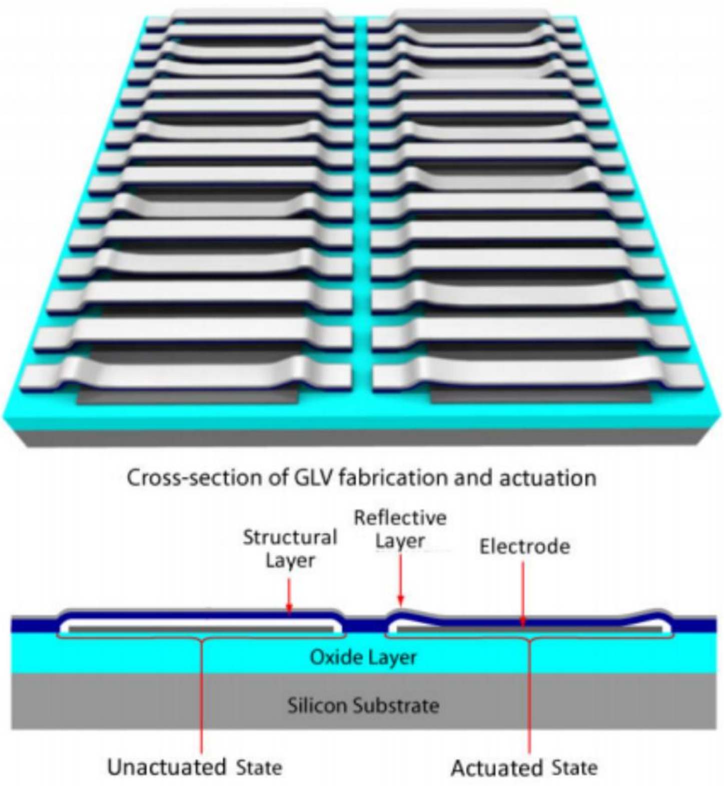

Figure 1.3 SCREAM process diagram

Into the 21st century, the range of applications for MEMS sensors has expanded rapidly, extending from the automotive sector (e.g., anti-lock braking systems and electronic stability control systems) to consumer electronics (e.g., gyroscopes and accelerometers in smartphones) and medical devices (e.g., miniature blood pressure sensors) [18−20]. Today, MEMS technology is a key component of IoT and AI devices, and continues to spawn new application scenarios such as smart homes, wearables and driverless technology through its integration with 5G and edge computing. This development has not only driven performance improvements and cost reductions in MEMS sensors, but has also led to tremendous market opportunities and technological innovations.

Nanoscience is the study of substances that are close to or slightly above the atomic and molecular level, that have special electrical and chemical properties, and that are smaller than 100 nm in size. Nanoscience includes nanophysics, nanochemistry, nanobiology, nanoelectronics, nanomechanics, nanofabrication and nanomaterials, etc. ~~Because these materials and devices and systems are close to the atomic or molecular scale, the technology of studying them is called nanotechnology.~~ Because these materials, devices, and systems are close to the atomic or molecular scale, the techniques used to study them are called nanotechnology, and furthermore, because the properties of nanoscale materials are different from those of bulk materials, nanotechnology is the study of the different and interesting properties of matter due to the effect of small size. Of course, of all the fields related to nanotechnology, there are four dominant areas of research that have not yet subsided: nanomaterials, nanoelectronics, nano biomedicine, and nanoelectromechanical systems (NEMS) [21]. Nanoelectromechanical systems (NEMS) refer to devices and systems with a size of 1-100 nm, featuring electromechanical integration and based on new effects of nanoscale structures. In terms of electromechanical systems, NEMS are the development and extension of MEMS. When the feature size reaches the nanometre scale, new effects such as small size effect, quantum size effect, surface effect, etc. are exhibited and many new special properties are derived that are not found in conventional solids.

In 2008, Guowei Chen of North Central University and Rong Zhu of Tsinghua University designed and fabricated a ZnO nanowire-based resonant silicon accelerometer, which consists of a ZnO nanowire resonator as the sensitive unit[22]. The experimental results show that the sensitivity of the accelerometer is an inverse function of the thickness of the silicon nanowires, and the sensitivity of the accelerometer can reach more than 2.5 kHz/g by choosing a thickness of 500 nm as the theoretical analysis data.

In 2010, Dzμng VietDao et al. from Ritsumeikan University obtained silicon nanowires with the narrowest width of about 128 nm by using SIMOX technology, and used the silicon nanowires to fabricate a micro-accelerometer with a very small size (500 × 500 × 400 μm3), with a sensitivity of 50 μV/g and a resolution of 30 mg under laboratory conditions. Figures 1.4 and 1.5 show the principle's model and the physical diagram of the accelerometer, respectively[23].

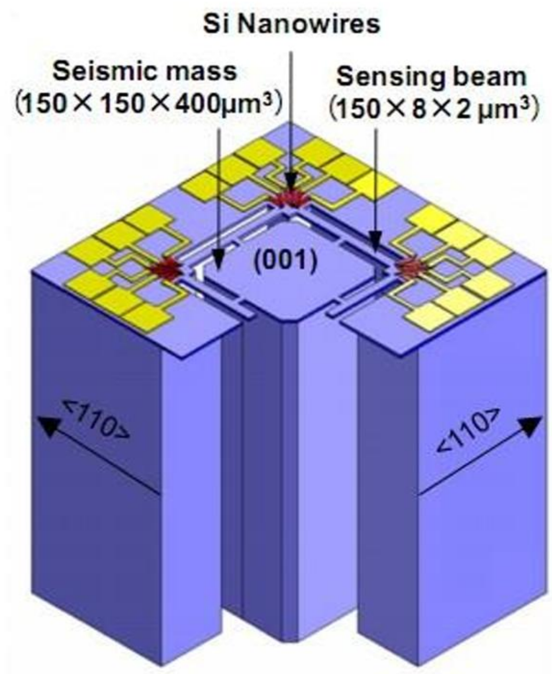

Figure 1.4 Principle model of silicon nanowire accelerometer Figure

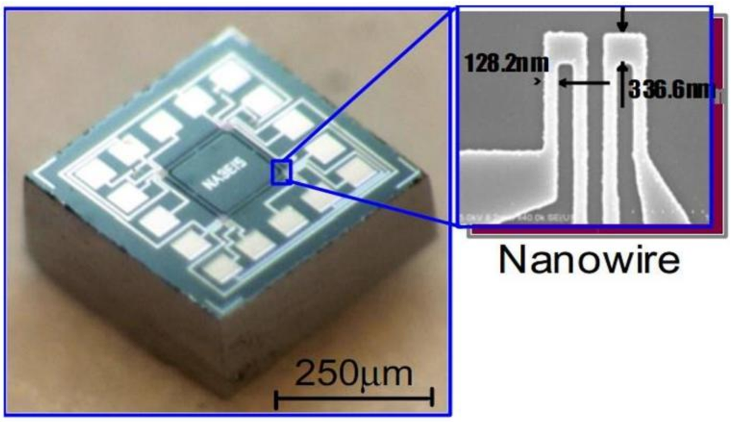

Figure 1.5 Physical diagram of silicon nanowire accelerometer

In 2010, Marta et al. from IMB-CNM, Spain, produced silicon nanowires with high mechanical and piezoresistive properties using a gas-liquid-solid mechanism, and documented the preparation of a cantilever beam accelerometer sensor using this silicon nanowire array using an electron microscope[24]. Based on the test result curves the conduction sensitivity was estimated to be $10^5 m^{-1}$, which is at least one order of magnitude higher than the conventional piezoresistive cantilever beams. A schematic of the sensitive structure of the sensor designed by Marta et al. and a curve of the relationship between the cantilever beam deformation and the nanowire resistance are shown in Figs. 1.6 and 1.7. According to the literature description, the sensor simply increases the number of nanowires used for the sensitive stress in the form of nanowire clusters which results in higher sensitivity.

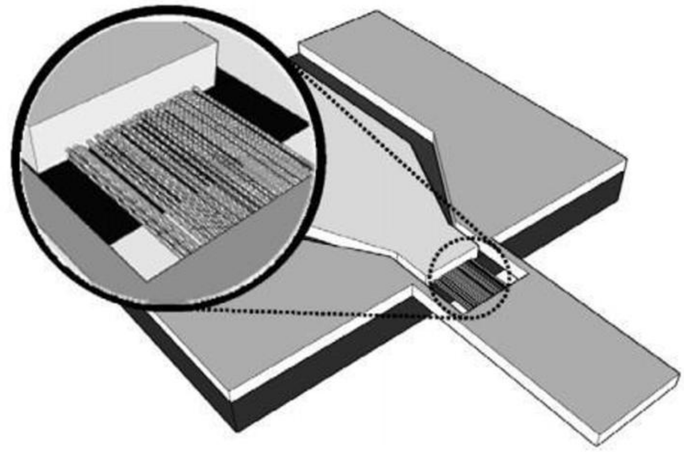

Figure 1.6 Schematic structure of the sensor for stress testing

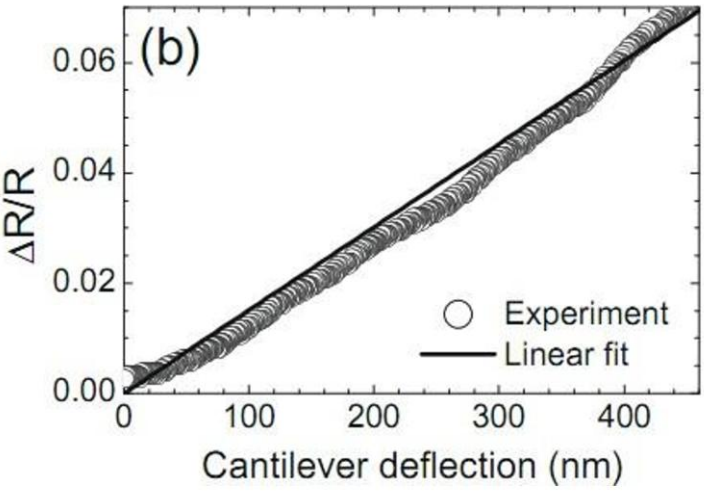

Figure 1.7 Curve of cantilever beam curvature versus rate of change of resistance

In 2010, GAO Chen et al. from Fudan University successfully prepared a silicon nanowire gas sensor with a sensitive line width of 22 nm by combining a 3-layer nanoimprint and wet etching process, and the resulting SEM photo of the silicon nanowire is shown in Figure 1.8[25]. Experiments were conducted by placing the device samples in NO2, and although the conductivity increased after the nanowires adsorbed NO2, the sensitivity of the gas sensor was only 14.7%, which was relatively low, and the current response curve is shown in Figure 1.9.

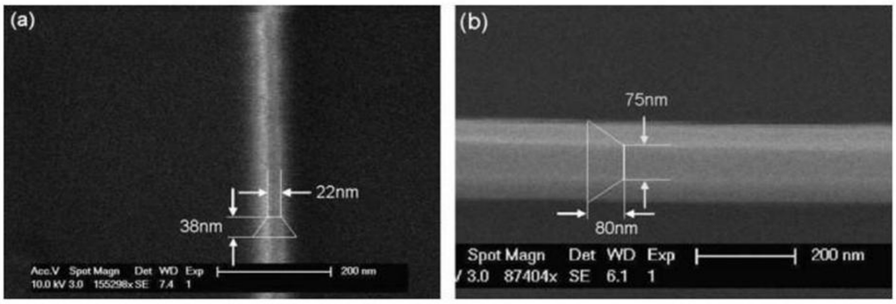

Figure 1.8 SEM photographs of silicon nanowires with tip linewidths of 22 nm and 75 nm

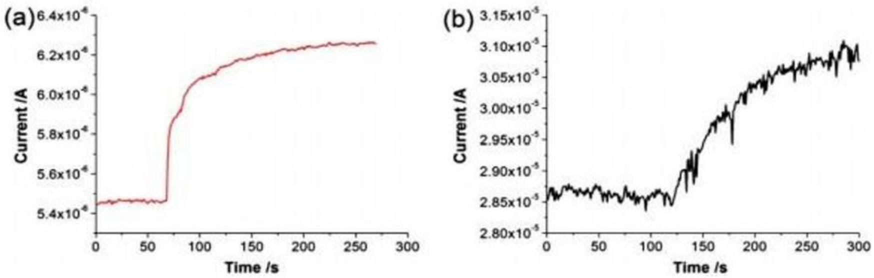

Figure 1.9 Current response curve of silicon nanowires

In 2011, Liang Loμ et al. at the National University of Singapore made a NEMS pressure sensor using a silicon nitride (SiN) and silicon nanowire integrated bilayer film, as shown in Fig. 1.10, which was fabricated with a length of 1 μm, a width of 100 nm and a thickness of 100 nm[26]. The paper concludes that the silicon nitride (SiN) and silicon nanowire integrated bilayer film doubled the sensitivity compared to the previous single-layer silicon nitride film.

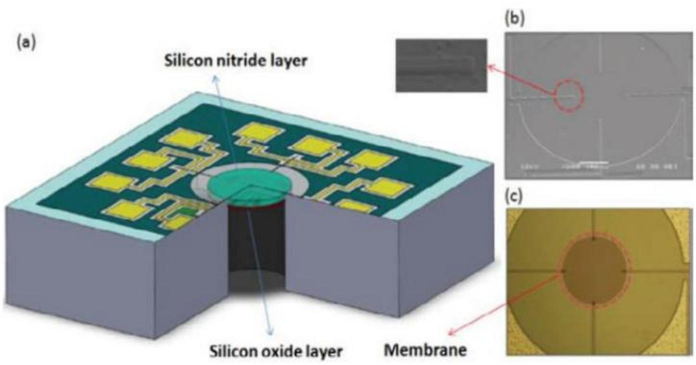

Figure 1.10 (a) Structural model of NEMS sensor; (b) SEM photo of silicon nanowire; (c) optical photo of thin film

In 2014, A. Shakarami et al. from Islamic Azad Mniversity, Iran, simulated and analysed silicon nanowire MEMS pressure sensors, and after varying the length, placement and other parameters of the silicon nanowires, compared with commercial MEMS pressure sensors concluded that, as shown in Table 1, the silicon nanowire MEMS pressure sensors are sensitivity is 19 times higher[27]. This proves the feasibility of silicon nanowire application in force sensitive devices in theoretical simulation.

Table 1: Silicon Nanowire MEMS Pressure Sensors vs. Conventional MEMS Sensors

Parameter	Symbol	Press. Sensor		Unit
		MOTOROL Silicon Balk	Silicon Nanowire	
Diaphragm Dimension	-	1000	1000	μm
Differential Pressure range	P_{OP}	100	100	kPa
Supply Voltage	V_S	3.0	3.0	Vdc
Supply Current	I_O	6	0.364	mAdc
Sensitivity	ΔV/ΔP	0.6	6.44	mV/kPa

In 2015, Lu Na et al. from Shanghai Institute of Microsystems and Information Technology designed and fabricated a COMS-integrated ultra-sensitive detection of dual carcinogens silicon nanowire array sensor chip, in which a single nanowire is 25 μm long and 80 nm wide, and the SEM photo and the silicon nanowire array photo are shown in Fig. 1.11 and Fig. 1.12, respectively[28].

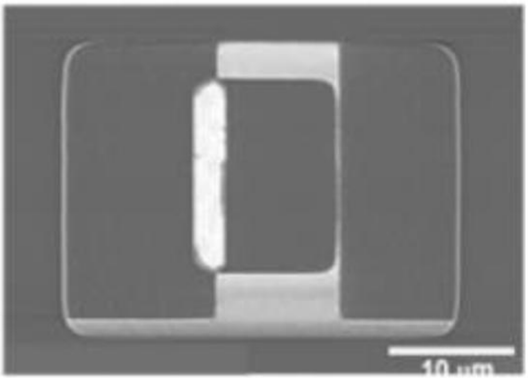

Figure 1.11 SEM photograph of silicon nanowire

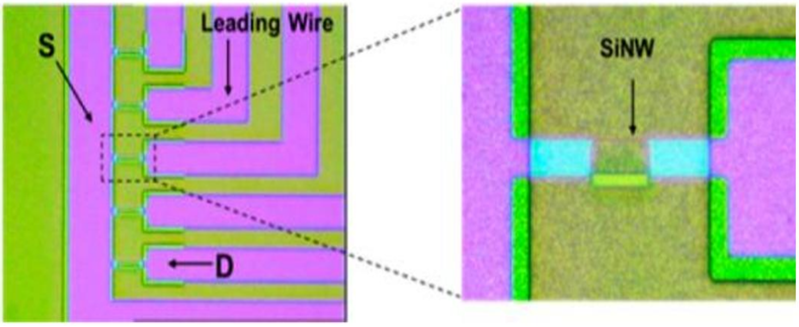

Figure 1.12 Microscopic image on chip

In summary, based on the above research status it is not difficult to find that silicon nanowires and their sensing applications are the hotspots of research in the field of micro-nano at home and abroad in recent years.

1.2 Main Objective

Based on the issues mentioned, this study proposes the design of a MEMS accelerometer utilizing a silicon nanowire array that capitalizes on its giant piezoresistive effect for vibration sensing. The high bandwidth properties of silicon nanowires enhance the sensor's performance in high-frequency vibration environments. The nanowire array converts the detected vibrations into resistance changes, which are collected in real time by front-end circuits for data conversion and preprocessing. The target sensitivity is set between 0.01 Ω/g and 0.05 Ω/g, where 0.01 Ω/g is suitable for precise measurements of small accelerations, ideal for high-accuracy applications, and 0.05 Ω/g ensures the feasibility and performance required in consumer electronics or low-cost products. The bandwidth ranges from 10 kHz to 20 kHz, making it applicable in various dynamic measurement scenarios, such as mechanical vibration and impact testing. The sensor operates stably within a temperature range of -40°C to +85°C, with temperature drift controlled within ±1%. These goals not only meet practical requirements but can also be realized in the initial design phase, with further performance improvements achievable through optimization in later stages.

1.3 Dissertation Overview

Combined with the investigated domestic and international research status, this dissertation aims to explore how to realise high-performance acceleration sensing devices using silicon nanowire structures under MEMS systems, and to enhance their comprehensive performance in terms of miniaturisation, low power consumption and integration. On the basis of the above, the finite element simulation software COMSOL is used to simulate silicon nanowire arrays, mass blocks and substrates with different feature sizes, and the top-down silicon nanowire fabrication method developed by Yang Xun's team is used to prepare silicon nanowire acceleration sensors, and finally, the performance of the silicon nanowire sensors is tested in kind. For the above research content, the chapters of this paper are arranged as follows:

Chapter 1 is the introductory part, which introduces the concept of MEMS sensors, the background of their development and their wide application in modern industrial and consumer electronics, illustrating their importance in automotive electronics, mobile phones and medical devices. This is followed by a brief introduction to the NEMS system, an extension of MEMS, and the current development of silicon nanowire sensor applications. Finally, the main design objectives of this paper and its significance are briefly stated.

Chapter 2 goes into the situation at the moment with MEMS sensors, which are certainly not without their challenges and limitations for various operational purposes like seismic monitoring, material selection, and car vibration avoidance, presents the operation theory of micro-acceleration sensors, exposes the sensitivity of the distribution that influences the performance heavily, as well as shows some of the latest research achievements and experimental results of MEMS accelerometers. This chapter not only gives the first-hand information for the future studies in the subsequent papers but also points out why it is necessary to solve the current technical problems.

Chapter 3 is the research method part, which explores the impact of material selection on device performance and the importance of material parameter settings in simulation software. It describes how to determine the dimensions and structure of each part of the accelerometer device, and explores the specific impact of dimensions on sensor performance. It explores the differences between the four different fixing methods and the specific impact on the sensor. It clarifies the specific steps and advantages of the top-down manufacturing method of silicon nanowires. This chapter clearly details the main content of my research work, technical details, theoretical basis, and the problems encountered and how they were solved.

Chapter 4 is the experimental results and discussion chapter. The specific performance parameters and application scenarios of the designed silicon nanowire sensor are analysed in detail through simulation and experiments, including the sensitivity of the acceleration sensor, the maximum operating acceleration, the frequency response, and the piezoresistivity coefficient. A comparison and discussion with traditional MEMS acceleration sensors is also provided. The results are discussed and possible errors are analysed.

Chapter 5 is the conclusion and outlook chapter, which summarizes the main technical achievements of this thesis, reviews the device advantages and innovations of this sensor, analyzes the remaining problems and improvement methods, and finally envisages the direction of future optimization.

2 Literature review

2.1 Current problems with MEMS accelerometers

Accelerometers are key devices in the MEMS field, designed to detect changes in the acceleration of objects within dynamic environments[29]. Due to their small size, low power consumption, and high integration, accelerometers have found widespread applications in consumer electronics, aerospace, industrial monitoring, and more. For example, in smartphones, they are used for screen rotation and gaming controls; in aerospace, they assist in flight attitude control and navigation; and in industrial monitoring, they are used for vibration monitoring and equipment fault diagnosis. However, as application scenarios continue to diversify, the limitations of traditional accelerometers' performance are becoming more apparent[30−31].

Trade-off between Sensitivity and Bandwidth： Accelerometers often face a trade-off between sensitivity and bandwidth[32]. For instance, in earthquake monitoring, sensors need to be highly sensitive to detect minute ground movements, but increasing sensitivity often results in a significant reduction in bandwidth, limiting the response to fast vibrations or high-frequency signals. This issue becomes particularly noticeable in complex dynamic environments, such as monitoring high-frequency vibrations in

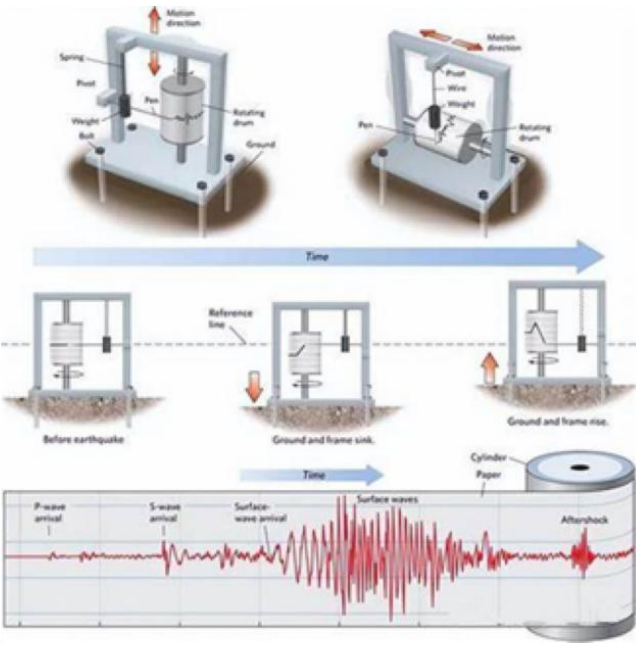

Figure 2.1 Seismic Sensor Schematic

machinery or shock testing in Figure 2.1. While the seismic sensor achieves high sensitivity, its design inherently attenuates high-frequency signals.

Material Limitations：Traditional accelerometers commonly use polysilicon as the sensing material like the pressure sensor in Figure 2.2. However, polysilicon exhibits weak piezoresistive effects, making it difficult to effectively detect small changes in acceleration. Additionally, the mechanical properties and thermal stability of the material limit its use in extreme environments[33].

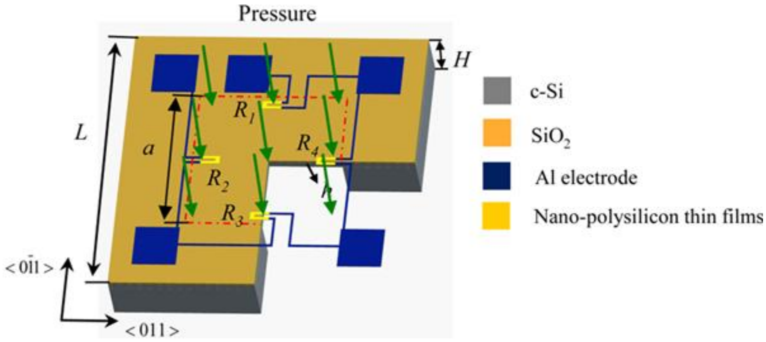

Figure 2.2 Based on nano-polycrystalline silicon thin-film pressure sensor

Challenges in Meeting Specific Scene Requirements：Certain application scenarios have particularly demanding performance requirements for sensors[34]. For example, in the suspension system of autonomous vehicles in Figure 2.3, sensors must not only be sensitive to high-frequency vibrations but also have a broad bandwidth to accommodate complex dynamic responses. Traditional sensors struggle to meet these needs, limiting their further application expansion.

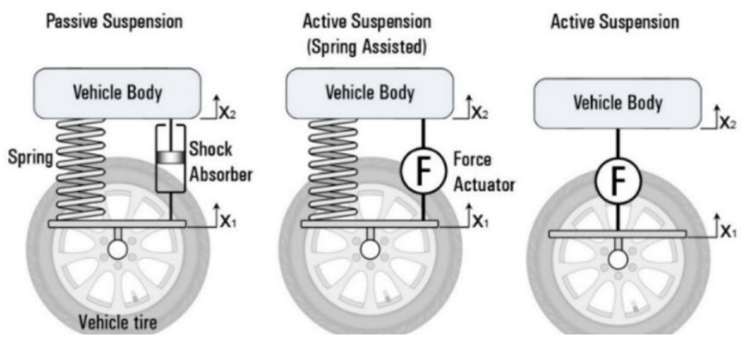

Figure 2.3 Schematic diagram of the active suspension operation of a smart car

2.2 Micro Accelerometer Working Principle

The working principle of the accelerometer sensor can be represented by the micro-accelerometer model diagram shown in Figure 2.4, which is equivalent to a second-order mass-spring-damping system. In the equation: M represents the mass of the mass block, D is the damping coefficient including the damping of the mechanical support structure and the membrane damping, K is the elastic stiffness coefficient, x is the displacement of the mass block relative to the sensor frame, and a is the acceleration of the sensor[35].

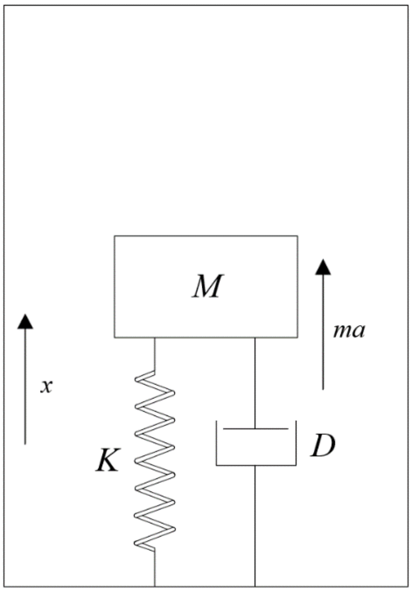

Figure 2.4 Diagram of the micro-accelerometer model

The measurement principle of the silicon nanowire piezoresistive accelerometer utilizes the displacement caused by the inertial mass under external acceleration, which induces deformation in the nanowire. Due to the piezoresistive effect, this deformation results in a change in the internal resistance of the nanowire. By measuring the change in the piezoresistive resistance of the nanowire, and using known piezoresistive coefficients and geometric parameters, the strain on the nanowire can be calculated, and the external acceleration can be determined based on the mechanical model. This device achieves high sensitivity, low power consumption, and miniaturized integrated acceleration measurement by leveraging the mechanical-electrical performance coupling at the micro-nano scale[36-37].

2.3 Sensitivity Distribution

To better reflect the entire process from force application to output signal in a micro-accelerometer, the overall sensitivity of the micro-accelerometer can be divided into two components: structural sensitivity and effect sensitivity.

Structural sensitivity refers to the relationship between the deformation of the accelerometer structure under external acceleration and the acceleration itself. The higher the structural sensitivity, the more sensitive the accelerometer is to acceleration and the more accurately it can measure acceleration.

Effect sensitivity refers to the relationship between the change in the output signal of the accelerometer and the external acceleration. High effect sensitivity means that the accelerometer can produce a larger change in the output signal, which helps improve detection sensitivity and signal-to-noise ratio.

These two sensitivities metrics together determine the performance of the accelerometer. Structural sensitivity focuses on the structural characteristics of the accelerometer itself, while effect sensitivity focuses on the relationship between the output signal change and the actual acceleration. When designing and evaluating MEMS silicon nanowire accelerometers, both metrics need to be considered to ensure the accelerometer has good sensitivity and accuracy[38].

2.4 Piezoresistive principle

2.4.1 Piezoresistive effect and scale

The piezoresistive effect was discovered by Smith in 1954 in the semiconductor materials silicon and germanium [39]. Applying stress to semiconductor materials, in addition to deformation, the energy band structure will change accordingly, the material is characterised as a change in semiconductor resistivity, which leads to a change in the resistance value, and this phenomenon of a change in the resistance value due to the action of stress is the piezoresistive effect [40]. Piezoresistive effect is a widely used sensor principle in the field of MEMS in modern society, such as accelerometers, pressure sensors, and other force-sensitive devices and inertial devices .

Any material deforms under the action of a force, and the deformation disappears with the force when it ceases to act; this deformation is called elastic deformation. The simplest deformation is the application of pressure or tension in any direction, called uniaxial stress. As shown in Fig. 2.5(a), a force fn applied to a sample in a direction perpendicular to the surface deforms the sample in the direction perpendicular to the force, as shown by the dotted line in the figure; conversely, if a pressure is applied, the sample shortens. The force per unit cross-section is called the stress T, i.e.

$$T = \frac{fn}{S}$$

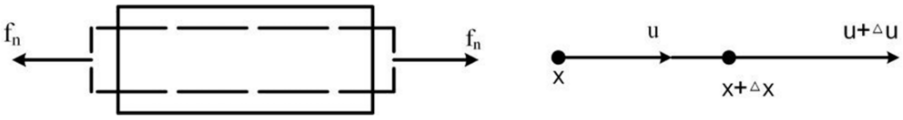

(a) Uniaxial stress (b) Longitudinal strain

Figure 2.5 Schematic diagram of uniaxial stress and longitudinal strain

where s is the cross-sectional area of the sample.

When the sample is deformed, a displacement occurs at a point within the sample, S. S is a function of position x, y, and z, and its three components are denoted by u, v, and w. When a pressure or a tension is applied, the displacement of a point within the sample is called the uniaxial stress and longitudinal strain. When pressure or tension is applied to any of the two points x and x+Δx (shown in Figure 2.5(b)) , the displacement of x in the x-direction during deformation is u, and the displacement of the point x+Δx is u+Δu then Δu/Δx is defined as the strain along the x-direction and is called the longitudinal strain, which is denoted by exx . If Δx→0, then

$$exx = \frac{\partial u}{\partial x}$$

Within the elastic limit, there is a proportional relationship between the strain-stress, i.e.

$$e = \lambda T$$

λ becomes the coefficient of elasticity. Introducing the concept of modulus of elasticity, E=1/λ, then

$$T = Ee$$

For longitudinal stretching, denote Young's modulus by E.

shown in Fig. 2.5(a), the transverse area of the sample narrows during longitudinal tensile deformation; conversely, the transverse area widens during longitudinal compressive deformation, then the relationship between the transverse deformation $\partial v/\partial y$ and the longitudinal stress T is

$$\frac{\partial v}{\partial y} = \beta T$$

β is called the transverse compression coefficient for longitudinal deformation. The ratio of β to λ is called Poisson's ratio v, i.e.

$$v = \frac{\beta}{\lambda}$$

Similarly, if a force ft is applied in the direction tangent to the sample, then stretching or compression occurs in the tangential direction. The ratio of the displacement in the y direction to Δx is called the shear strain $\partial v/\partial x$. As shown in Figure 2.6.

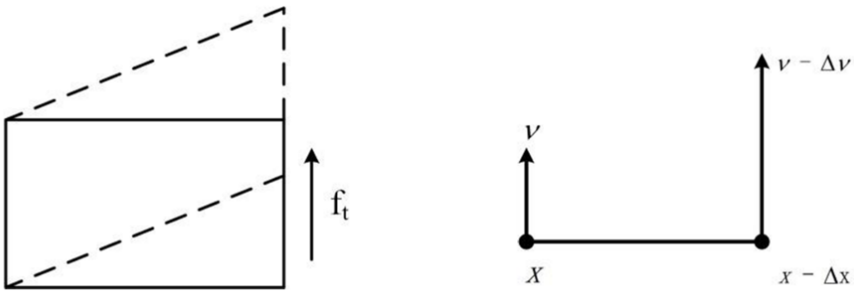

(a) Uniaxial stress (b) Longitudinal strain

Figure 2.6 Tangential Stress and Tangential Strain

The formula for calculating the resistance of a sample material of length l and cross-sectional area s(πr^2) is:

$$R = \rho \frac{l}{s}$$

The resistance value is determined by the overall resistivity ρ and the geometry. Therefore, it can be seen by the equation that there are two directions in which applying stress or strain changes the resistance value. First, changing the characteristic dimensions, both length and crosssectional area, will change with strain. When the applied stress is in the longitudinal direction, strain will follow in the transverse direction. If the resistive length increases, the cross-section at finite Poisson's ratio may decrease as well. Secondly, the resistivity of some materials may be a function of strain and change with strain. Both aspects will also be discussed below in the text.

When it is stretched by an external force F, l increases and s decreases, and the partial differentiation of the last formula reveals that R changes by the following amount:

$$dR = \frac{\partial R}{\partial l} dl + \frac{\partial R}{\partial s} ds + \frac{\partial R}{\partial \rho} \cdot d\rho$$

in the formula

$$\frac{\partial R}{\partial l} = \frac{\rho}{s}$$

$$\frac{\partial R}{\partial s} = -\rho l \frac{1}{s^2}$$

$$\frac{\partial R}{\partial \rho} = \frac{l}{s}$$

Substituting into equation yields

$$dR = \frac{\rho}{s} \cdot \left(dl - l \cdot \frac{ds}{s} \right) + \frac{d\rho}{s}$$

since s=πr^2 , ds=2πrdr, i.e.

$$\frac{ds}{s} = 2\frac{dr}{r}$$

then we have

$$\frac{ds}{s} \cdot \frac{l}{dl} = \frac{2\frac{dr}{r}}{\frac{dl}{l}} = 2\frac{\varepsilon r}{\varepsilon} = -2\mu$$

Eq. where εr=dr/r is the transverse or radial strain of the material; ε=dl/l is the axial or length or longitudinal strain of material; μ=-εr/ε is Poisson's ratio, which is the fixed ratio of the relative shrinkage of the transverse linearity to the relative elongation of the longitudinal linearity.

Substituting equations and dividing both sides by R yields

$$\frac{dR}{R} = \varepsilon \cdot (1 + 2\mu) + \frac{d\rho}{\rho} = (1 + 2\mu + \frac{\frac{d\rho}{\rho}}{\varepsilon}) \cdot \varepsilon = K0 \cdot \varepsilon$$

where K0=1+2μ+(dρ/ρ)/ε is the sensitivity factor, which is the rate of change of resistance due to unit strain.

The relative change in electrical resistance of semiconductor materials in response to an external force is the same as for metals, with an expression as in Eq., and since the relative change in resistivity of semiconductor materials is proportional to the stress σ, i.e.

$$\frac{d\rho}{\rho} = \pi\sigma$$

where π is the piezoresistive coefficient of the material.

From Hooke's theorem, the relationship between the stress σ and the strain ε on the material is

$$\sigma = E\varepsilon$$

where E is the modulus of elasticity.

Substituting Eq. yields

$$\frac{d\rho}{\rho} = \pi E\sigma$$

$$\frac{dR}{R} = \varepsilon \cdot (1 + 2\mu) + \frac{d\rho}{\rho} = (1 + 2\mu + \pi E) \cdot \varepsilon = K0 \cdot \varepsilon$$

For metallic materials, the effect of πE on the rate of change of resistance is very small or even negligible, and the Poisson's ratio μ=0.25 ~ 0.5, so K1=1+2μ ≈ 1~2 in Eq. For semiconductor materials, the effect of 1+2μ on the resistance change rate is negligible, and common semiconductor materials such as silicon, germanium, etc., have a very small or even negligible effect on the resistance change rate $\pi = (40 \cdot 10^{-11} \sim 80 \cdot 10^{-11})m^2/N$ and the modulus of elasticity of the material $E = 1.67 \cdot 10^{11} N/m^2$ then Eq. has the following equation

$$K2 = \pi E = 50 \sim 100$$

it can be seen that

$$K2 = 50K1 \sim 100K1$$

From the above equation, it can be seen that the sensitivity coefficient of the semiconductor material is 50-100 times larger than that of the metal material, which is the reason why semiconductor materials are commonly used as sensitive elements in MEMS sensors nowadays. From equation, it can be seen that

$$\frac{dR}{R} = \frac{d\rho}{\rho} = \pi\sigma$$

It shows that the relative rate of change of the resistance value of the semiconductor material is equal to the relative change of the resistivity, and the calculation of the piezoresistive coefficient in the text is carried out according to this formula.

2.4.2 Calculation of piezoresistive coefficient

Monocrystalline silicon is a kind of each anisotropic material, the piezoresistive coefficient of different crystal direction is different, so the orientation is different while its characteristics are also not the same. The crystal direction is the representation of orientation, the so-called crystal direction is the direction of the normal of the crystal surface[]. Let X, Y and Z be Monocrystalline silicon crystal silicon. There are two ways to represent the crystal orientation in a plane, as shown in Figure 2.7.

(1) Intercept

can be expressed by equation

$$\frac{X}{r}+\frac{Y}{s}+\frac{Z}{t}=1$$

where r, s, and t represent the intercepts of the X, Y, and Z axes, respectively.

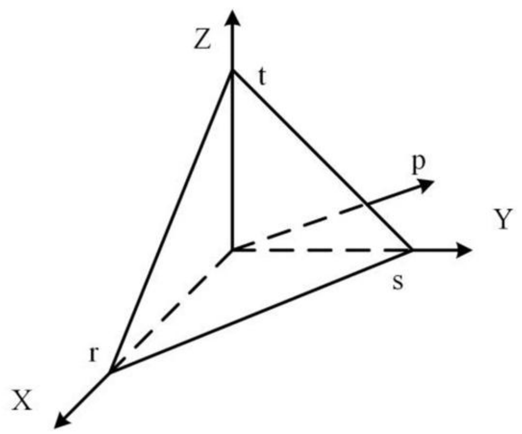

Figure 2.7 Plane intercept representation

(2) Normal equation

can be expressed by equation

$$X\cos\alpha+\mathrm{Y}\cos\beta+\mathrm{Z}\cos\gamma=p$$

where p is the normal length;

cosα, cos β, cos γ - the cosine of the direction of the normal, which can also be expressed as l, m, n.

If the magnitude of the normal p is known, the cosine of the direction of the normal can be expressed as l, m, n.

If you know the size and direction of the normal p (i.e., the direction cosine), you can determine the plane. If only the direction but not the magnitude of the normal p is known, only the direction of the plane is determined.

If these two equations represent the same plane, then we have

$$\frac{X}{p}\cos\alpha + \frac{Y}{p}\cos\beta + \frac{Z}{p}\cos\gamma = 1$$

$$\cos\alpha : \cos\beta : \cos\gamma = \frac{1}{r} + \frac{1}{s} + \frac{1}{t}$$

It can be seen that if the intercepts r, s, and t of the crystal plane in stereo coordinates are known, the directions of the normals 14 Dissertation, North Central University The cosine can then be found. Thus, the direction of the normal can be determined. By taking the inverse of the three intercepts r, s, and t in equation are reduced to integers h, k, and l, respectively, which have no convention and are called Miller indices. There are

$$\cos\alpha : \cos\beta : \cos\gamma = h : k : l$$

From equation it is possible to determine the normal direction, the crystal direction as the normal direction of the crystal plane, after the crystal direction is known, the crystal plane can be determined. In China, the <hkl> method is used to represent the crystal direction, the (hkl) method is used to represent the crystal plane, and the ｛hkl｝ method is used to represent the crystal plane family.

Figure 2.8 (a) shows the plane and the X-axis, Y-axis, Z-axis intercept of -2, -2, 4, the inverse of the intercept of -1/2, -1/2, 1/4, Miller's index is 221, so its crystal direction, crystal plane, crystal plane family are <221>, (221), {221}. The intercepts of the plane shown in Fig. 2.8(b) with the X-axis, Y-axis, and Z-axis are 1, 1, 1, and the inverse of the intercepts is still 1, 1, 1, and the Miller index is 111, so its crystallographic direction, crystal plane, and crystal plane family are <111>, (111) and {111}, respectively. The ABCD shown in Fig. 2.8(c) has an intercept of 1, ∞ and ∞. The intercepts of the ABCD plane are 1,1/∞, 1/∞, the inverse of the intercepts are1, 1, 1, and the Miller index is 100, so the crystal directions, crystal planes, and crystal face families of the ABCD plane are <111>, (111),{111}, respectively. Similarly, the orientation, facets and families of BEFC are <010>, (010), {010}, and the orientation, facets and families of CFGD are <001>, (001), {001}.

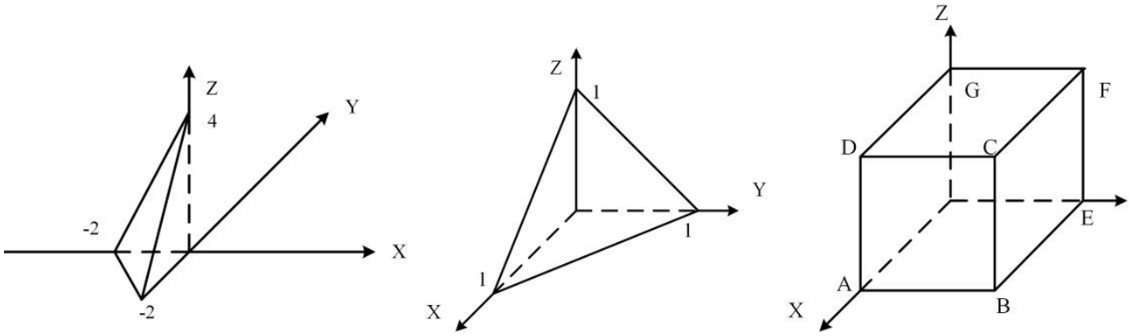

(a) (b) (c)

Figure 2.8 Orientation and Facet Diagrams

Since the properties of ABCD, BEFC and CFGD are the same in cubic crystals, <100>, <010> and <001> are sometimes used interchangeably, <001> can be used to express <100>.However, for the same single crystal, due to the different distribution of atoms on different faces, the physical properties of each face are different, and naturally the size of piezoresistive effect is also different. MEMS sensors usually choose the crystal direction with the largest piezoresistive effect to arrange the resistor strip, and the commonly used crystal directions are <001>, <011>, and <111>, and the piezoresistive effect is usually diffused in these three crystal directions.

Since silicon is a cubic crystal system, the direction of the coordinate axis is the same as the direction of the crystal axis, as shown in Figure 2.9. The six external forces that change the resistivity of the cubic crystal system are indicated in the figure, i.e., the axial stresses T1, T2, T3 along x, y, z and the stresses T3 parallel to the yz, zx, xy surfaces, respectively, around x, y, zx, xy and zx. T4, T5, T6 and the shear forces T4, T5, T6 which are parallel to the yz, zx, xy surfaces and cause them to rotate about the x, y, z axes, respectively. The relative change in resistivity is $(\Delta\rho/\rho)1$, $(\Delta\rho/\rho)2$, $(\Delta\rho/\rho)3$, such that the change in resistivity on the yz, zx, xy shear surfaces of The relative change is $(\Delta\rho/\rho)4$, $(\Delta\rho/\rho)5$, $(\Delta\rho/\rho)6$, since there are stresses that cause changes in resistivity only in certain directions, the relationship between the relative change in resistivity and stress is commonly expressed in the following inertia matrix as

$$\begin{bmatrix} (\Delta\rho/\rho)1 \\ (\Delta\rho/\rho)2 \\ (\Delta\rho/\rho)3 \\ (\Delta\rho/\rho)4 \\ (\Delta\rho/\rho)5 \\ (\Delta\rho/\rho)6 \end{bmatrix} = \begin{bmatrix} \pi_{11} & \pi_{12} & \pi_{12} & 0 & 0 & 0 \\ \pi_{12} & \pi_{11} & \pi_{12} & 0 & 0 & 0 \\ \pi_{12} & \pi_{12} & \pi_{11} & 0 & 0 & 0 \\ 0 & 0 & 0 & \pi_{44} & 0 & 0 \\ 0 & 0 & 0 & 0 & \pi_{44} & 0 \\ 0 & 0 & 0 & 0 & 0 & \pi_{44} \end{bmatrix}$$

When a stress is applied to single crystal silicon, the resistance of the silicon crystal changes due to piezoresistive effect. The relative change in resistance dR/R versus stress is shown in equation. In an orthogonal coordinate system, the coordinate axes are aligned with the crystal axis when there is

$$\frac{dR}{R} = \pi_l\sigma_l + \pi_t\sigma_t + \pi_s\sigma_s$$

Where:

σ_l - longitudinal stress;

σ_t - transverse stress;

σ_s - stress perpendicular to the longitudinal and transverse stresses;

π_l - coefficient of longitudinal piezoresistance;

π_t - transverse piezoresistive coefficient;

π_s - the piezoresistive coefficient perpendicular to the longitudinal and transverse directions.

Since σ_s is much smaller than σ_t and σ_l , it is generally omitted. π_l means that the current through the element is in the same direction as the direction of stress; π_t means that the current through the piezoresistive element is perpendicular to the direction of stress.

When there is a deviation between the crystal axis of a silicon crystal and the crystal axis of a cubic crystal, the rate of change of resistance is expressed as

$$\frac{dR}{R} = \pi_l\sigma_l + \pi_t\sigma_t$$

In this case, the values of π_l , π_t in Eq. can be expressed as π_{11} , π_{12} , π_{44} as

$$\pi_l = \pi_{11} - 2(\pi_{11} - \pi_{12} - \pi_{44})({l_1}^2{m_1}^2 + {l_1}^2{n_1}^2 + {n_1}^2{m_1}^2)$$

$$\pi_t = \pi_{12} + (\pi_{11} - \pi_{12} - \pi_{44})({l_1}^2{l_2}^2 + {m_1}^2{m_2}^2 + {n_1}^2{n_2}^2)$$

Where:

$\pi_{11}, \pi_{12}, \pi_{44}$ - longitudinal, transverse and shear piezoresistive coefficients of the piezoresistive element, which are three independent piezoresistive coefficients of semiconductor materials such as silicon and germanium.

l_1, m_1, n_1- the cosine of the longitudinal stress of the piezoresistive element with respect to the cubic crystal axis;

l_2, m_2, n_2 - the cosine of the transverse stress of the piezoresistive element with respect to the direction of the cubic crystal axis, respectively.

The piezoresistive coefficients of different types of monocrystalline silicon at room temperature are shown in Table 2.

Table 2: Piezoresistive Coefficients of Common Silicon Materials

Piezoresistivity ($10^{-11}Pa^{-1}$)	N-type (Resistivity=11.7 $\Omega \cdot cm$)	P-type (Resistivity=7.8 $\Omega \cdot cm$)
π_{11}	-102.2	6.6
π_{12}	53.4	-1.1
π_{44}	-13.6	-138.1

2.4.3 Factors affecting the piezoresistive coefficient

In contrast to the silicon piezoresistive coefficient of bulk silicon, the factors affecting the piezoresistive coefficient of silicon nanowires are no longer limited to the diffuse impurity's surface concentration and ambient temperature; at the nanoscale, the nature of a substance depends not only on its shape but also on its size.

(1) Doping concentration

Figure 2.9 shows the curves of the resistivity of silicon at 300K as a function of impurity concentration [41]. The two curves in the figure are P-type and N-type silicon, respectively, versus the doping concentration N of the surface impurities. For light doping (impurity concentration $10^{16}\sim10^{18}cm^{-3}$), the resistivity is simply inversely related to the impurity concentration, the higher the impurity concentration, the lower the resistivity, which is approximated as a straight line in Fig. 2.9[42]. When heavily doped, that is, the impurity concentration increases, the curve is no longer a straight line, a serious deviation, the main reason may be two aspects: on the one hand, the impurities at room temperature and can't be fully ionised, in the heavily doped simple semiconductors is more serious; on the other hand, the mobility with the increase in the concentration of the impurity decreases significantly.

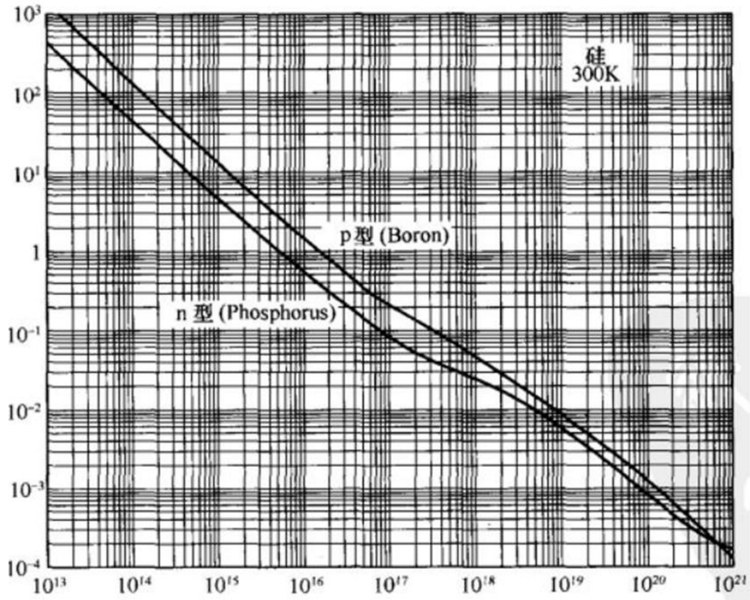

Figure 2.9 Plot of silicon resistivity versus impurity concentration

(2) Geometry

There is a certain size dependence in the material properties when the semiconductor size reaches down to the nanoscale, one of the reasons for this is that the specific surface area increases as the scale decreases to the nanoscale, the specific surface area plays an important role as most of the physicochemical reactions take place on the surface, therefore, semiconductors have better overall material properties when they have a larger specific surface area.

2.5 Cutting-edge research directions in MEMS

The current cutting-edge research in MEMS accelerometers focuses on several key areas[43]. These include the development of highly sensitive sensors through advanced materials like silicon carbide, graphene, and carbon nanotubes, which offer better mechanical and electrical properties[44]. For example, the accelerometer shown in Fig.2.10 uses a dual-mass block system, two supporting beams, a hinge beam, and four tiny piezoresistive self-supporting beams. By independently separating the piezoresistive sensor microbeams and support beams, the correlation between measurement sensitivity and resonance frequency is weakened. This design allows for improved sensitivity of the piezoresistive accelerometer without sacrificing the resonance frequency. The structural dimensions of the sensing chip were optimized through finite element simulation.

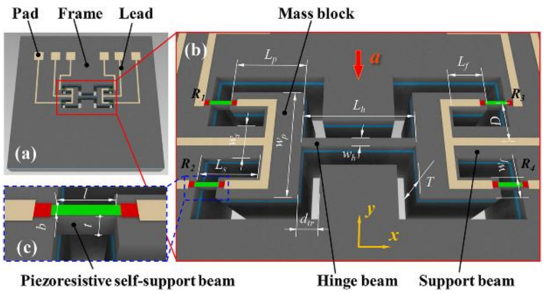

Figure 2.10 dual-mass block, support beam accelerometer

Low-power MEMS sensors are another crucial focus, especially for applications in IoT and wearable devices, where energy efficiency is vital[45].

There is also growing interest in multi-axis accelerometers, which can detect motion in multiple directions and are ideal for applications like robotics and 3D motion tracking[46]. The sensor in Figure 2.11 features a four-sided, four-fixed beam structure. Three sets of Wheatstone bridges are used to measure the X, Y, and Z-axis accelerations at the base of each beam. The resistors R1 to R4 form the Wheatstone bridge for the X-axis, R5 to R8 for the Y-axis, and R9 to R16 for the Z-axis. These three Wheatstone bridges independently measure the accelerations along the X, Y, and Z axis.

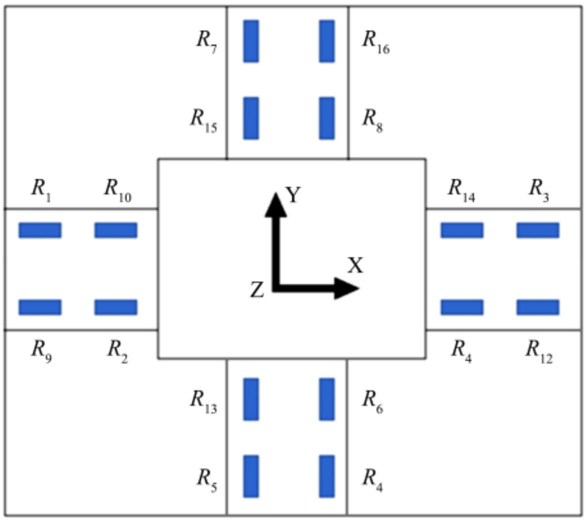

Figure 2.11 Three-axis resistive accelerometer

Integration of MEMS accelerometers with other sensors, such as gyroscopes and pressure sensors, is also a significant trend, enhancing the overall sensor performance.

Flexible and wearable MEMS accelerometers are being developed for health monitoring and human-machine interaction[47]. Similarly, the pressure sensor shown in Figure 2.12 features a two-layer structure. Initially, a single-walled carbon nanotube network is deposited on the surface-modified elastic membrane interface. Subsequently, conductive gold islands are bridged on the printed circuit board. By adjusting the design of the gold islands and the conductivity of the nanotube network, the sensor's linear detection range and sensitivity can be effectively controlled.

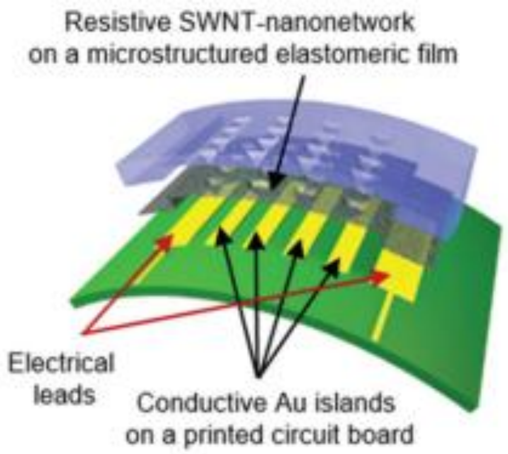

Figure 2.12 Pulse wearable pressure sensor

Research is also targeting MEMS sensors that can perform well in extreme environments, such as high radiation or high-temperature conditions, for use in aerospace and deep-sea exploration.

Additionally, the automotive industry is driving innovations in MEMS accelerometers for use in autonomous driving systems, ensuring safety and stability in real-time motion sensing[48-49]. These advancements are contributing to the widespread adoption of MEMS accelerometers across various industries.

MEMS technology was initially used for physical sensors, and among MEMS physical sensors, mechanical measurements have gained a lot of attention due to the development of robotics and the study of mechanics of various materials.

Makihata [50] proposed a capacitive tactile force sensor in (Fig. 2.13), in which reliable crystalline silicon was used as the sensing structure and a "MEMS-On-CMOS" process was developed to enable the sensor to have features that meet the basic CMOS wafer fabrication standards such as stacked integration, electrical feedthrough to the backside pad, etc., meeting basic CMOS wafer fabrication standards.

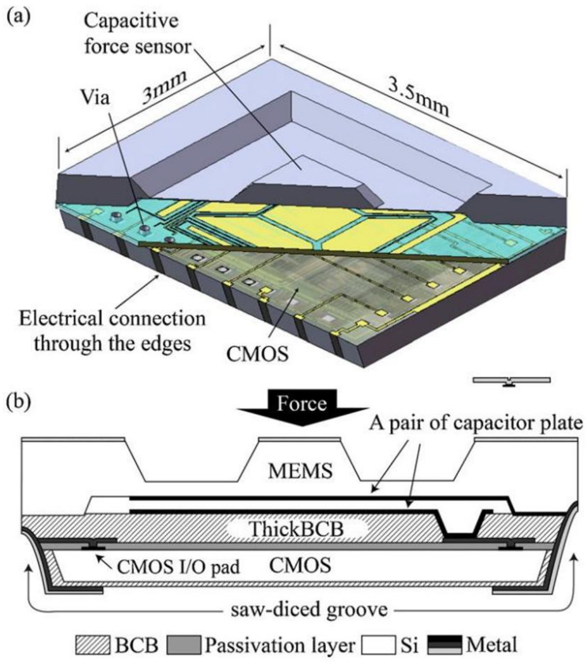

Figure 2.13 Plot of silicon resistivity versus impurity concentration

In order to characterise the mechanics of biomaterials, H.J. Pandya [51] in showed that the mechanical properties of biomaterials can be improved by using laboratory insulators on silicon.A silicon piezoresistive cantilever beam force sensor capable of measuring forces in the range of μN~nN was designed and fabricated by Silicon On Insulator (SOI). fabricated cantilever beam was 130 μm long, 40 μm wide, and 1.0 μm thick.A series of force-displacement curves of the prepared micro-cantilever beam were obtained using a commercial AFM, and the data were analysed to obtain the spring constant and sensitivity of the micro-cantilever beam, which were 0.1488 N/m and 2.7 mV/N, respectively.

Engineered superhydrophobic surfaces are highly promising materials for many industrial applications such as self-cleaning, external machine coatings, etc. In order to understand the sliding mechanism of droplets on superhydrophobic surfaces, a 2-axis piezoresistive force sensor based on MEMS technology was proposed by Nguyen Thanh-Vinh [52] in (Fig. 2.14). The sensor is capable of directly measuring the interaction force of a water droplet during sliding on a superhydrophobic surface through an array of micropillars.

A metre-sized column underneath serves as the sensing element. Two piezoelectric resistors were formed at the roots of two opposing silicon beams to detect forces acting on the column surface in both normal and tangential directions. The resolution of the sensor for both normal and tangential forces is less than 20 nN, which is sufficient to measure the force acting on a droplet on the microcolumn. The prepared sensor was able to measure the interaction force of a 7.5 μL droplet as it slid on the microcolumn array.

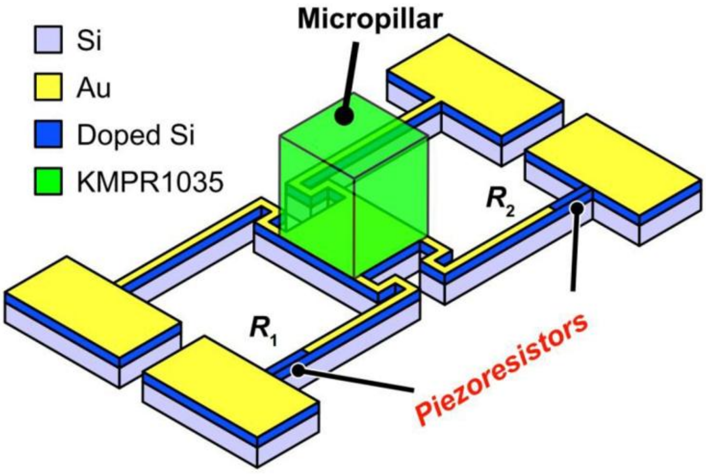

Figure 2.15 A piezoresistive MEMS force sensor

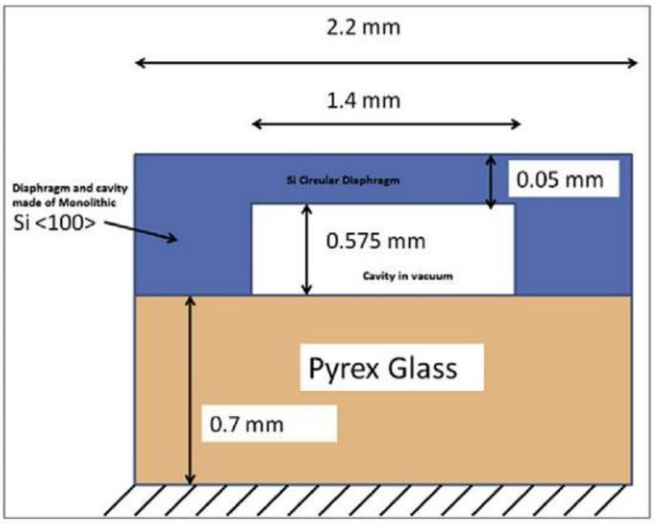

Figure 2.14 Cross-section of the force sensing cell of a MEMS force sensor

Utilising the property of monocrystalline silicon piezoresistors with a measurement factor of up to 200, Rajesh Kumar [53] designed a circular MEMS diaphragm load sensor a capacity of 50 N in (Fig. 2.15), where a unique combination of thin monocrystalline silicon diaphragms was used as the mechanical sensing element. The force sensor consists of four piezoresistors in a wheelstone bridge structure that converts the applied force into an electrical quantity (e.g., a voltage), and the force is in the range of 10-50 N. The sensitivity of the sensor ranges from about 0.35 to 0.40 mV/V/N.

In order to suppress residual stress distortion and improve sensitivity, Meng-Lin Hsieh [54] fabricated a novel capacitive CMOS-MEMS haptic sensor with a vertically integrated sensing structure and discrete sensing arrays in (Fig. 2.16). The tactile sensor utilises a cushioning polymer above the sensor and a polymer filled between the vertically integrated sensing structures as a force transmission layer, which allows for effective force loading onto the sensor, and more importantly, simultaneous deformation of the two vertically integrated sensing structures during force loading, which ensures an increase in sensitivity for the same footprint. Furthermore, in order to mitigate possible distortion problems caused by residual stresses in the film, the sensor is discretised into an array of individual sensing units, which are electrically connected in parallel to ensure maximum capacitive signals. Compared to a reference tactile sensor using conventional sensing electrodes, the designed sensor achieved a sensitivity of 5.61 fF/N, an improvement of nearly 1.3 times.

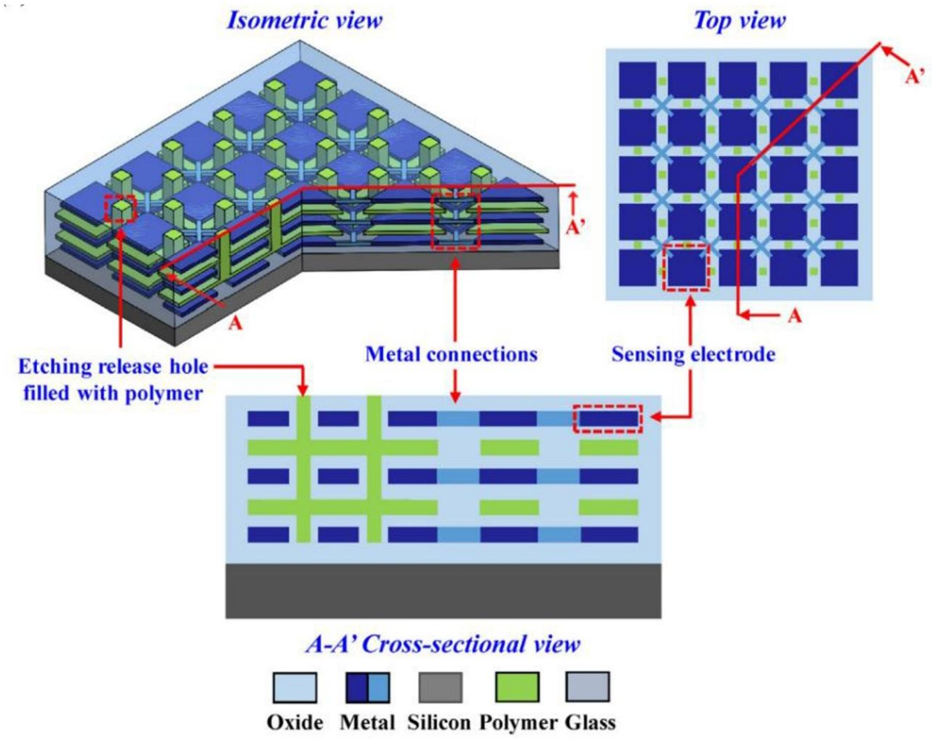

Figure 2.16 Isometric, top and cross-sectional views of a MEMS tactile force sensor

3 Research Methodology

3.1 Material selection

The choice of P-type single-crystal silicon for the sensitive mass block in Figure 3.1 and N-type single-crystal silicon for the silicon nanowires in Figure 3.2 is based on their complementary electrical properties, which enhance the sensor's sensitivity. P-type and N-type silicon exhibit different electrical characteristics, allowing for more efficient strain-induced changes in resistance when exposed to acceleration. This difference enhances the sensor’s overall performance, especially in terms of the piezoresistive effect, which is crucial for accurate acceleration measurement.

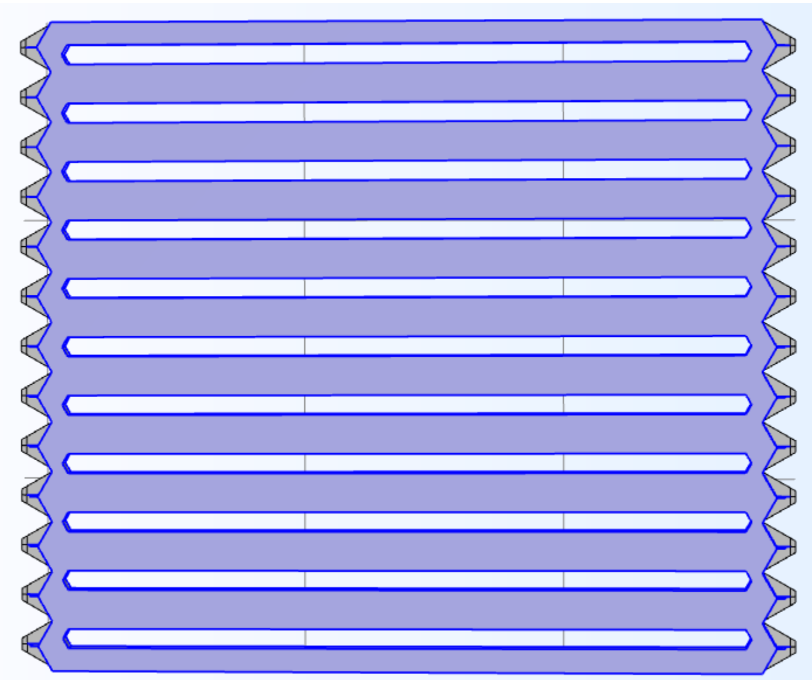

Figure 3.2 The p-type silicon mass block (purple part)

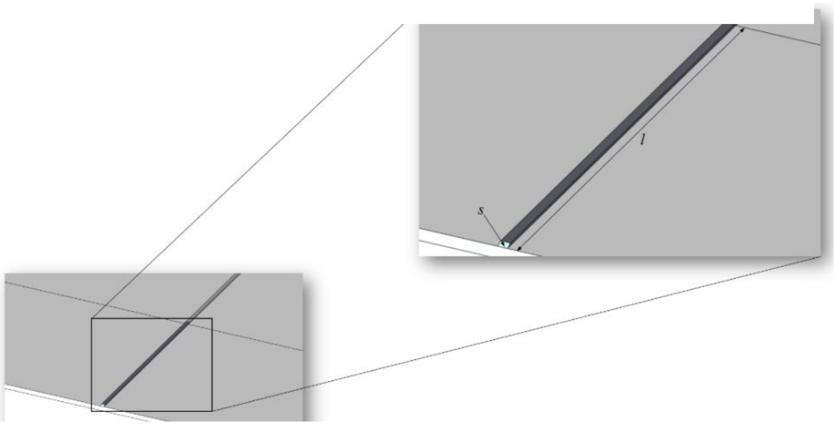

Figure 3.1 silicon nanowires

The use of Si_3N_4 (silicon nitride) for the substrate and cantilever beams in Figure 3.3 is due to its superior mechanical properties, such as high hardness and compressive strength. Silicon nitride's low thermal expansion coefficient ensures that the sensor remains stable even under varying temperatures, maintaining its reliability and performance over time. Additionally, Si_3N_4's insulating properties help reduce electrical noise, ensuring accurate measurements by minimizing signal interference.

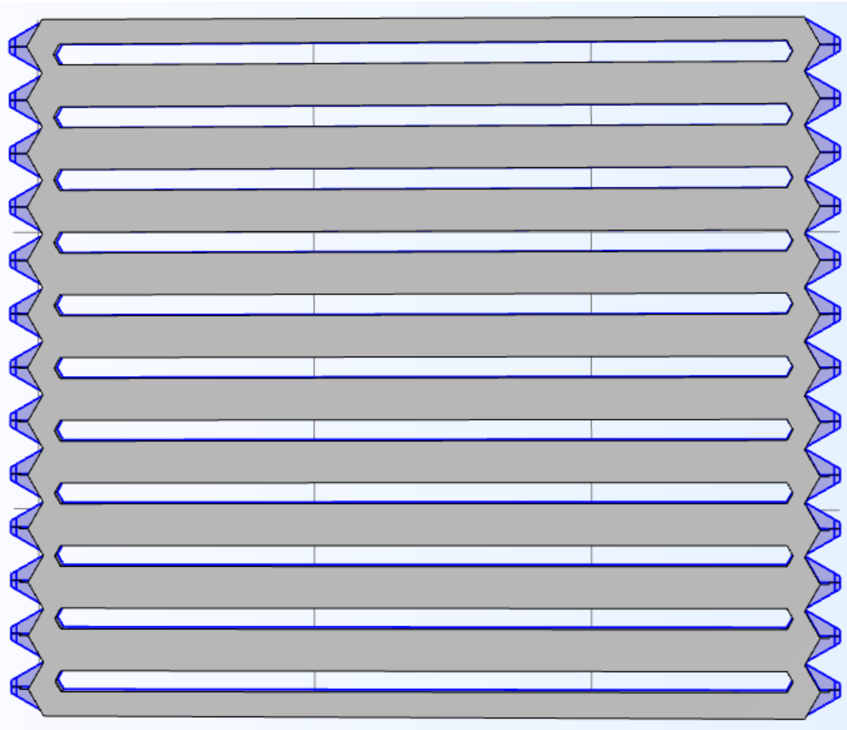

Figure 3.3 Si3N4 substrate (purple part)

Together, the P-type and N-type silicon complement each other to improve electrical response, while silicon nitride enhances the structural integrity and stability of the MEMS accelerometer.To ensure the accuracy of the simulation, isotropic Young's modulus values, which are consistent with silicon properties, were used in the simulation. The isotropic structural loss factor was set to 1/1000.

3.2 structural design

Extensive research has shown that silicon nanowires with diameters smaller than 50 nm exhibit significant quantum confinement effects, which can further enhance sensitivity. However, the fabrication process becomes considerably more challenging, with a substantial increase in the risk of fracture and a low yield rate of only 30% [14]. Duan et al. pointed out in their study that when the diameter of silicon nanowires exceeds 150 nm, the piezoresistive effect weakens significantly by approximately 60%, making it difficult to meet high-sensitivity sensing requirements [15]. In this study, the fabrication of silicon nanowires adopts the self-limiting oxidation process, as shown in Figure 3.4. When the oxidation time is set to 30 minutes, the diameter of the silicon nanowires stabilizes within the range of 81–103 nm, with a uniformity error of only ±15 nm [16].

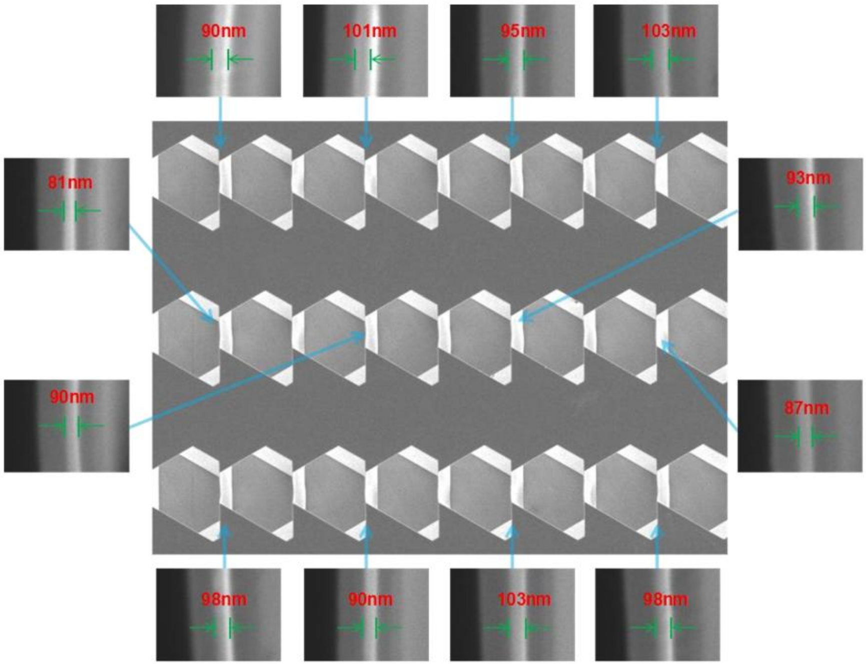

Figure 3.4 The distribution of silicon nanowires in the array

According to the piezoresistive theory, the resistance change rate of silicon nanowires can be expressed as:

$$\frac{\Delta R}{R} = \pi \cdot \sigma = \pi \cdot E \cdot \epsilon$$

Where π is the piezoresistive coefficient, E is the Young's modulus of silicon, and ϵ is the strain. When the diameter D of the silicon nanowire decreases, the strain ϵ under the same inertial force increases significantly ($\epsilon \propto 1/D$), thereby enhancing sensitivity. Based on this, this study selects an 80 nm silicon nanowire diameter, which is the result of systematic optimization considering process limitations, piezoresistive effect theory, dynamic reliability experiments, and literature comparisons. This choice provides a crucial guarantee for the high sensitivity and long-term stability of the accelerometer.

The resistance of the silicon nanowire, $R = \rho L/S$, increases linearly with length L. As shown in Figure 3.5, the resistance of a 5 μm-long silicon nanowire is relatively low, while at 17 μm, the resistance rises significantly to 34 kΩ. Excessive resistance increases thermal noise and reduces the signal-to-noise ratio, thereby affecting measurement accuracy. Moreover, longer silicon nanowires experience greater mechanical stress, making them more susceptible to external vibrations and temperature variations, which can compromise device reliability. Furthermore, due to etching, deposition, and doping constraints, excessively long nanowires may affect manufacturing consistency. Conversely, as shown in Figure 3.6, overly short silicon nanowires exhibit smaller strain, leading to insufficient sensitivity and reduced sensor detection capability. Therefore, this study selects 11 μm as the optimal length for a single silicon nanowire, balancing high sensitivity while avoiding signal degradation.

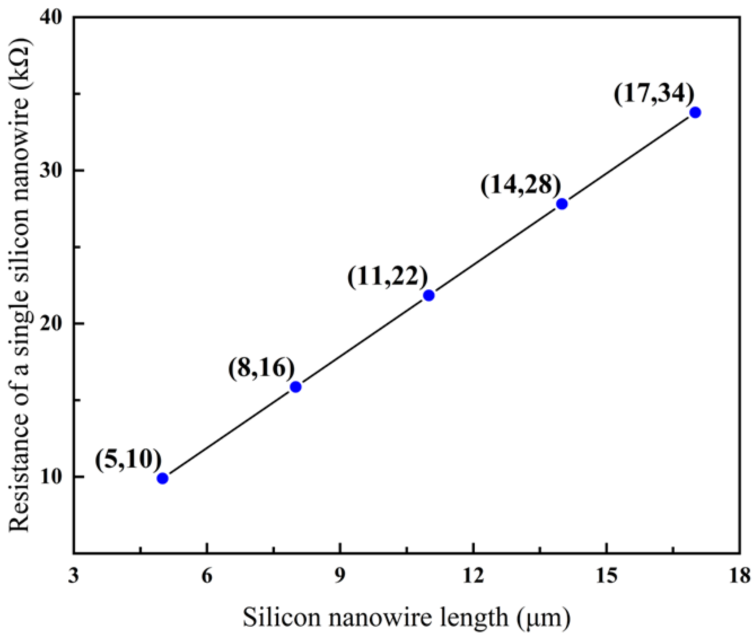

Figure 3.5 Resistance graph of a single silicon nanowire at different lengths

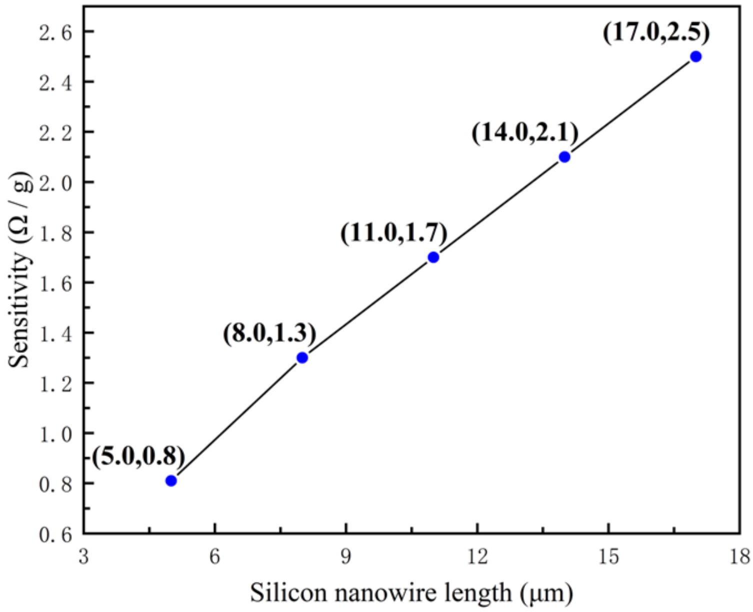

Figure 3.6 Sensitivity graph of a single silicon nanowire at different lengths

In this study, the silicon nitride capping layer thickness is set to 100 nm. The fabrication process adopts low-stress chemical vapor deposition (LPCVD) technology, ensuring uniform deposition while maintaining compatibility with CMOS processes [16]. Silicon nitride has a high Young's modulus of 250–300 GPa, and a 100 nm thickness is sufficient to withstand the dynamic load of silicon nanowires. Experimental results show that this thickness can increase device yield to over 90%. Additionally, 100 nm ensures insulation performance without significantly increasing gate capacitance, thereby maintaining high device response speed. In summary, the 100 nm silicon nitride capping layer achieves an optimal balance between process feasibility, mechanical properties, electrical performance, and chemical stability, providing a key safeguard for the reliability of this accelerometer.

Through simulation analysis of different numbers, lengths, cross-sectional areas of silicon nanowires, various sizes of the mass block, and the shapes of the substrate, specific size data for each part of the sensor was designed. This process took into account the balance between performance indicators, such as sensitivity, resonant frequency, and mechanical stability. By simulating changes in different parameters, the design of each component was optimized to maximize the overall function and performance of the sensor. These size data were refined and verified multiple times, ensuring that the sensor could achieve the best working state in practical applications, with high stability and accuracy.

3.3 Selection of Fixing Method

As shown in Figure 3.7, the silicon nanowire accelerometer has been successfully constructed and is fixed on both sides of the Si_3N_4 substrate at the bottom to ensure its stability.

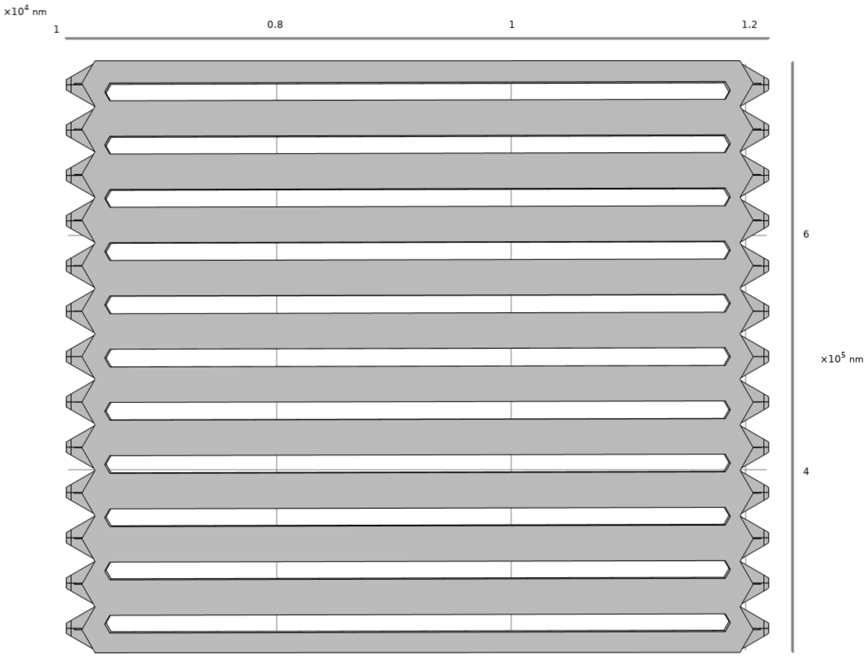

Figure 3.7 Silicon Nanowire Accelerometer Schematic

These four figures in Figure 3.8 respectively illustrate the simulation results of the accelerometer under different boundary conditions: single-sided fixation, full fixation, four-point fixation, and central double-ended fixation. After detailed analysis, the double-sided full fixation was selected as the optimal design.

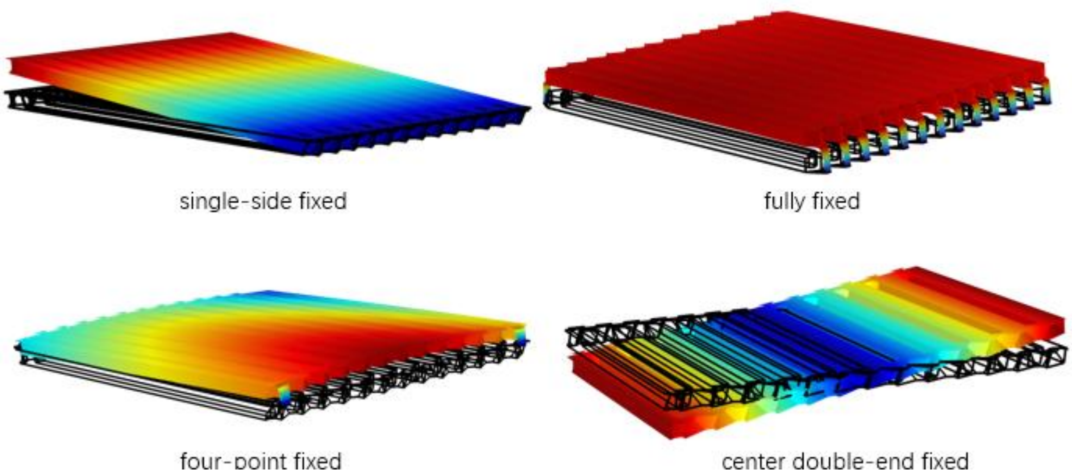

Figure 3.8 Four types of fixing methods

The single-sided fixation has certain limitations in structural rigidity, which may lead to inconsistent sensor readings. Although the full fixation enhances stability, it compromises flexibility, affecting the sensor's sensitivity. The four-point fixation improves stability but encounters challenges in achieving the desired resonant frequency and sensitivity.

In contrast, the double-sided full fixation provides the best balance between stability and performance. It constrains all structural boundaries, ensuring a more stable geometry and stress distribution, thereby reducing vibration, deformation, and stress concentration issues. Since all edges are fixed, the overall rigidity of the structure is maximized, minimizing displacement under applied force, effectively preventing excessive deformation that could affect measurement accuracy. Compared to single-sided fixation, four-point fixation, or central double-ended fixation, the full fixation mode significantly increases the natural frequency of the structure, reducing the likelihood of low-frequency resonance and ensuring sensor stability even in high-frequency vibration environments. Additionally, due to reduced degrees of freedom, the full fixation structure is less sensitive to external environmental interferences such as temperature variations and impact vibrations, thereby improving measurement reliability. After optimization, this design achieved the best performance across all measurement parameters, demonstrating superior reliability in practical applications.

3.4 COMSOL simulation environment construction

The modelling and simulation software used for the silicon nanowire acceleration sensor designed in this study is COMSOL. In contrast to other micro- and nanoscale modelling software, COMSOL's finite element method can support sub-micron geometric modelling, and it also has built-in modules dedicated to surface effects and quantum confinement effects, which is critical to the accuracy of the nanowire sensor.

When carrying out simulation and mechanical property analysis of silicon nanowires, the selection of the The selection of suitable material parameters is quite critical when carrying out simulation and mechanical property analysis of silicon nanowires. For P-type silicon nanowires, the Young's modulus is set to 170 GPa and Poisson's ratio is set to 0.23, which is mainly based on the following considerations:

the mechanical properties of silicon are obviously anisotropic, and the Young's modulus of single crystal silicon in different crystalline directions is generally between 130 and 188 GPa. In practical engineering applications or simulations, in order to simplify the model and to ensure the safety margin of engineering, researchers sometimes choose higher approximate values, such as 170 GPa. This value can guarantee the stiffness of the material under loading conditions, and can also reflect the local enhancement effect due to the surface effect and microstructure to a certain extent, the crystal structure of P-type silicon may have a slight change due to doping concentration, and the lattice distortion caused by doping will have a certain effect on the Young's modulus, and adopting the value of 170 GPa is often proved to be a better match with the actual measurement data. The use of 170 GPa has often been shown to be better in experiments than in actual measurements, and this value can compensate for possible parameter deviations in the model when nanoscale effects are considered.

Poisson's ratio is a key parameter to characterise the ratio of transverse deformation and longitudinal expansion of the material, for silicon, Poisson's ratio is generally taken between 0.22 and 0.28, and the value of 0.23 as the Poisson's ratio of P-type silicon is the average value based on a large number of experimental data and literature reports, and this value can accurately describe the transverse contraction of the silicon when it is subjected to the action of the stress, and the small change of Poisson's ratio may have a large effect on the strain distribution in the nanofabricated structure, and this value can compensate for the possible parameter deviation in the model when considering the nano-scale effect. In the micro-nano-machined structure, the small change of Poisson's ratio may have a large impact on the strain distribution, and a reasonable and commonly used value can ensure the reliability of the simulation results and the stability of the model. In addition, in the simulation analysis, parameter selection often needs to strike a balance between accuracy and simplicity of processing, due to the P-type silicon nanowire preparation process may exist crystal defects, surface oxide layer and other process factors, the use of 220 GPa and 0.23 as a standard parameter to facilitate the comparison of the results of the existing research, and can reduce the complexity of the simulation process, to improve the stability and reliability of the model solving. In summary, the Young's modulus of P-type silicon is set to 220 GPa and Poisson's ratio is set to 0.23, which is based on experimental data, literature analysis and experience in engineering practice, and this parameter can accurately reflect the mechanical response of silicon material in nano-scale in the simulation model, and at the same time, ensure that the computational process is simplified and the results have reference value.

In the setting environment of the solid mechanics field, the appropriate setting of the damping is of great significance for accurately reflecting the actual state of energy dissipation and the vibration characteristics of the system. I decided to set the damping of the linear elastic material as the anisotropic loss factor, and the specific value is 1/1000, the main reasons are as follows: 1/1000 of this value is in the category of the lower damping level, which is suitable for the performance of internal friction and the energy dissipation characteristics of the common materials, such as silicon, in the micro-scale state. The main reason is that the damping value of 1/1000 is at a low damping level, which is in line with the internal friction and energy dissipation characteristics of such commonly used materials in the microscale state. In many experiments and related literature, it is generally held that in most microelectromechanical structures, the damping effect is relatively small, and the use of 0.001 as the dimensionless loss factor can accurately simulate the actual situation. The isotropic loss factor indicates that the damping effect will be uniformly distributed in all directions, which is a reasonable assumption for most of the microstructured materials. This is a reasonable assumption for most microstructured materials, since in most cases the damping of the material does not show a strong anisotropic character. In this way, it can simplify the model calculation process and make the results more universal. Choosing the value of 1/1000 ensures that the simulation model maintains a stable state and the numerical solution can be converged smoothly, so that the system will not be decayed too quickly because of too much damping, and will not lead to numerical oscillations or problems of energy accumulation because of too little damping.

Elastic resistance refers to the change in resistance of a material when it is subjected to mechanical strain, and is also known as the piezoresistive effect. Silicon is a kind of material with outstanding piezoresistive effect, and under nanoscale conditions, given the size effect and surface influence, its resistance will become more sensitive to small strains, in the setup of silicon nanowires, I choose to set it as an elastic resistor, relying on the setup of silicon nanowires as an elastic resistive element, the stress or acceleration exerted by the outside world will trigger the silicon nanowires to produce a small deformation, resulting in a measurable change in resistance. resistance changes that can be measured. This characteristic is the key to detecting acceleration or vibration, and the effectiveness of the piezoresistive effect of silicon in the design of sensors has been demonstrated in a large number of literature and practical applications. The choice of an elastoresistive element allows for the construction of an accurate and stable sensing mechanism, which is suitable for both engineering and practical applications, with a number density of 1×10^{20} 1/cm^3, a high level of doping that reduces the number of dopants. This high doping level reduces the base resistance of the silicon nanowires, allowing the device to operate with good conductivity while still retaining enough piezoresistive effect to detect resistance changes induced by small stresses. High doping density keeps the material properties stable, reduces resistance fluctuations due to temperature changes or lattice defects, and improves the repeatability of the sensor as well as its long-term stability. Literature and experimental data illustrate that, in piezoresistive MEMS acceleration sensors, the doping concentration is generally between 1×10^{19} and 1×10^{20} 1/cm^3, a value that ensures the ideal conductivity and reliable piezoresistive response. Adopting the parameter of 1×10^{20} 1/cm^3 in the numerical simulation, an accurate and realistic elastic resistance model can be constructed, which provides a theoretical basis for the subsequent design optimisation.

For acceleration sensors, the fixed state of the sensor will have a direct impact on its structural rigidity and mechanical response. If the Si_3N_4 substrate in all acceleration sensors is fully fixed on the side, it will ensure that the sensors will have a uniform and stable boundary condition when they are subjected to external forces, and will greatly reduce the non-ideal strain distribution due to the insecurity of the fixation. This will greatly reduce the non-ideal strain distribution caused by insecure fixation and ensure the highest sensitivity and reliability of the signal output from the sensitive element, i.e., the silicon nanowire array. In terms of the fixation method, the full fixation of the Si_3N_4 substrate sides of all the accelerometers should be selected as mentioned above to provide stable and consistent boundary conditions, and the full fixation method guarantees the rigidity and stability of the structure when subjected to stresses and maximises the sensitivity.

In the simulation process, the reasonable application of loading conditions is the key to obtain accurate simulation results, a variable unit volume force load along the z-axis direction is uniformly applied to the sensor as a whole, which ensures that each unit volume inside the entire sensor is subject to the same acceleration. This can build a real mechanical environment, but also to ensure the consistency of the stress distribution in the simulation process, so that the subsequent sensitivity and response characteristics of the analysis has become more reliable. After the completion of the material modelling, property settings and physical field construction, the sensor is applied to the whole sensor in the z-axis direction of a variable unit-volume force load, so that the acceleration sensor is uniformly subjected to the same acceleration of each unit volume. The uniform loading conditions can truly reflect the mechanical response under the actual working environment and ensure the accuracy of the simulation data.

In finite element simulation, the quality of mesh delineation is directly related to the computational accuracy and efficiency, because the silicon nanowire array, as the main sensitive element, has a much smaller size than other structural components, and needs to be constructed individually with a finer and more detailed local mesh to capture small strain changes, whereas for the other components, in order to ensure the simulation efficiency as well as the stability of the overall model, a uniform standard mesh is used. A hierarchical mesh strategy is used to ensure computational efficiency while maintaining the necessary simulation accuracy. To this end, a fine, independent mesh is applied to the small and critical silicon nanowire arrays, while a uniform standard mesh is applied to the auxiliary structures. This approach balances the high accuracy of the core components with the global simulation performance, optimises the use of computational resources, and improves the overall efficiency of the model solution.

3.5 Top-down preparation method

Although the ‘bottom-up’ preparation method can prepare a large number of silicon nanowires, it cannot achieve highly precise and controllable preparation, and it is difficult to transfer and position them, which greatly limits their large-scale application. The top-down preparation method uses a photolithography process to achieve accurate positioning of the silicon nanowires, which can meet the high stability and repeatability of the silicon nanowire device preparation process. Therefore, this type of preparation method can achieve the controlled preparation of silicon nanowires in batches.

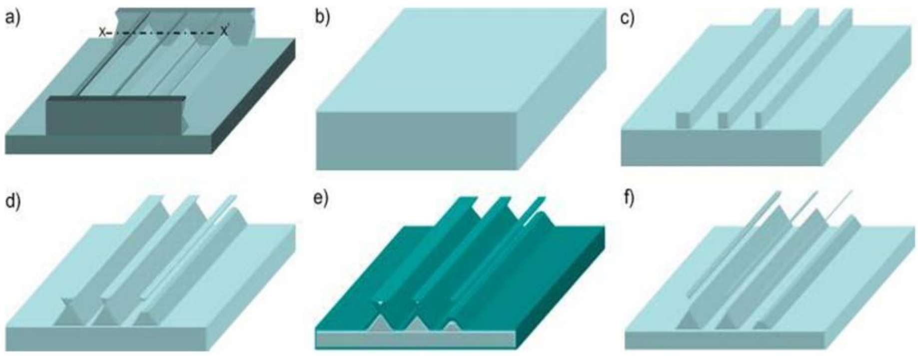

Figure 3.9 Flow chart of the preparation method of single crystal silicon nanowires based on (100) silicon wafers.

The commonly reported ‘top-down’ preparation methods mostly use processing techniques such as electron beam lithography and deep ultraviolet lithography. As shown in Figure 3.9, the preparation method of silicon nanowires based on ordinary (100) silicon wafers uses an expensive deep ultraviolet lithography machine [57]. This preparation method transfers nanometer-scale pattern structures through a deep ultraviolet lithography machine, and then an anisotropic etching of the silicon is used to prepare a columnar structure with an isosceles triangle cross-section. After self-limiting oxidation, an unoxidised area is left in the centre of the columnar structure, which is the silicon nanowire. Finally, the silicon oxide is removed to obtain a suspended silicon nanowire structure as shown in Figure 3.9f.

As shown in Figure 3.10, this figure is a flow chart of the preparation method of single crystal silicon nanowires based on (110) silicon wafers. This method uses ordinary (110) silicon wafers [58], first an anisotropic etching is performed using TMAH silicon etching solution to prepare vertical silicon grooves, and then an isotropic etching is performed to thicken the walls between the silicon grooves to 300 nm. Finally, the silicon nanowires are prepared by self-limiting oxidation. This method uses isotropic etching to thicken the silicon wall structure, but the control accuracy of this process is not high, making it difficult to prepare silicon walls with a consistent width across the entire wafer. This ultimately leads to difficulty in achieving uniformity in the dimensions of the silicon nanowires.

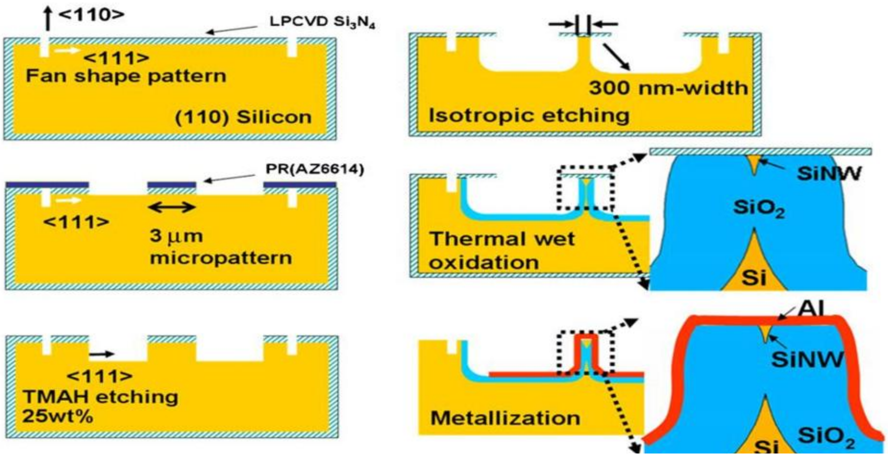

Figure 3.10 Flow chart of the preparation method of a single crystal silicon nanowire based on a (110) silicon wafer.

As shown in Figure 3.11, using SOI silicon wafers, Hien Duy Tong and others precisely and controllably prepared silicon nanowires by controlling the angle of dry etching [59]. However, because the silicon nanowires were directly prepared using dry etching, the surface of the silicon nanowires was too rough, which affected the performance of the silicon nanowire device. In addition, the silicon nanowires produced using SOI wafers tend to be attached to the oxide layer. When the silicon nanowires are used as the sensitive part of a sensor, the oxide layer on the surface of the silicon nanowires needs to be removed, but the oxide layer at the bottom of the silicon nanowires is also removed at the same time. As a result, the silicon nanowires are in a completely suspended state, and the silicon nanowires lacking a protective structure are extremely prone to breakage. Most of the existing ‘top-down’ preparation methods require the use of expensive equipment, and the control accuracy of the width of the silicon nanowires is not high enough. The prepared silicon nanowires lack of a protective structure leads to a lack of long-term stability of the device, so there is an urgent need to develop a low-cost preparation technology with high controllability and precision and a simple process.

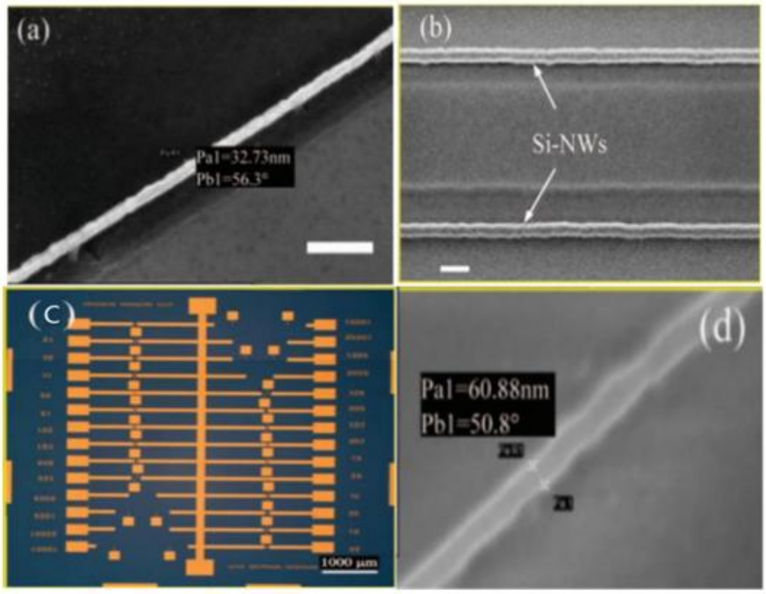

Figure 3.11 Preparation of silicon nanowires can be controlled by controlling the dry etching angle.

3.6 Method for preparing an array of silicon nanowires

In fact, most of the current signals generated by single-silicon nanowire devices reported in the literature are in the nanoampere range. Such weak signals place high demands on the test circuit and often require the use of expensive testing equipment. However, practical applications require low-cost, mass-produced and reproducible devices, and it is clear that single-silicon nanowire devices are not yet able to meet these requirements. Arrays of silicon nanowires, in which many silicon nanowires are connected in parallel between two electrodes, can effectively solve the problem of weak test signals. When a silicon nanowire array sensor is working, the signals of multiple silicon nanowires are superimposed on each other, which strengthens the output current signal. In theory, the more silicon nanowires that are connected in parallel, the stronger the overall signal. Therefore, the number of silicon nanowires can be increased to amplify the measured signal, thereby effectively improving the signal strength and stability of the sensor. There have been few reports on the controllable preparation of silicon nanowire arrays, and there are still many technical problems with the relevant preparation processes that need to be urgently solved. The following is a summary of the currently reported silicon nanowire array preparation techniques.

The methods for preparing silicon nanowire arrays can also be divided into two categories: bottom-up and top-down.

(1) Bottom-up method for preparing silicon nanowire arrays: This method uses chemical vapor deposition (CVD) to grow silicon nanowires from gaseous or vaporous substances on the gas-solid interface under the action of a metal nanoparticle catalyst. The CVD-prepared silicon nanowires are disordered, and an ordered arrangement method (such as the template method or Langmuir-Blodgett technology) is required to achieve a regular distribution of silicon nanowires [60,61]. As shown in Figure 3.12, using a nano-scale alumina channel as a template, silicon nanowires can only grow within the confined template channel. The alumina template can effectively limit the diameter, growth position and growth direction of the nanowires during the growth process.

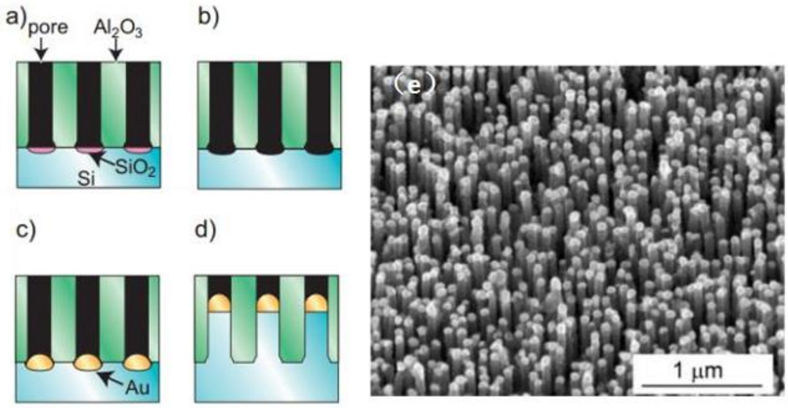

Figure 3.13 Stencil method in combination with CVD.

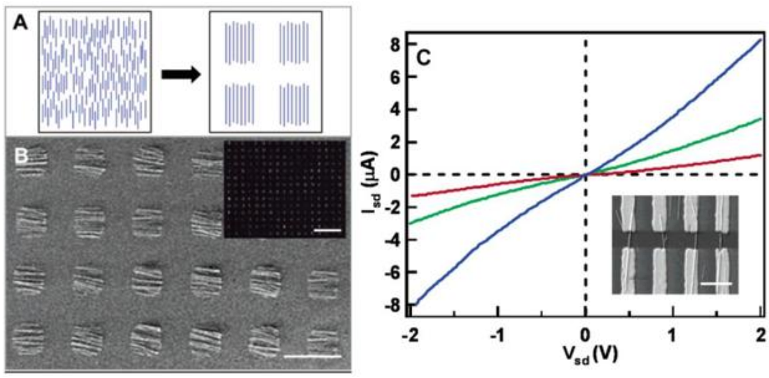

Figure 3.12 Langmuir-Blodgett technique in combination with CVD.

At present, there are two main methods for preparing ordered silicon nanowire arrays from the top down:

The first method is metal-catalysed chemical etching (MACE), which involves the use of a corrosion solution to etch specific areas of the silicon wafer under the catalytic action of metal nanoparticles to simply and quickly prepare large-area, highly oriented silicon nanowire arrays [62]. As shown in Figure

3.14, this figure shows the reaction flow chart for preparing silicon nanowire arrays by the MACE method. In the first step, Ag particles are deposited on the surface of the silicon wafer: Ag+ is reduced to Ag atoms after receiving electrons, and Ag atoms aggregate to form nanoparticles and deposit on the surface of the silicon wafer. In the second step, the silicon nanowire array is formed by etching. The Ag particles are used as catalysts to oxidise the Si below the Ag particles to SiO2. The SiO2 is then dissolved by the etching solution, the Ag particles sink, and the above process continues to form vertical pits, finally forming a silicon nanowire array as shown in Figure 3.15. Metal catalytic chemical etching 7 Preparation and application research of highly controllable silicon nanowire array devices The preparation of silicon nanowire arrays is inexpensive and simple to operate, but since the morphology of the silicon nanowires cannot be prepared in a controlled manner, the size of the silicon nanowires is difficult to accurately control. The resulting silicon nanowires often have a large size deviation and there is a phenomenon of adhesion. Therefore, when this silicon nanowire array is used as the sensitive element of a sensor, it is difficult for the measured object to quickly enter the silicon nanowire array, which results in a long response time of the sensor. At the same time, due to the lack of a protective structure, the silicon nanowires are extremely prone to breakage, and the device lacks long-term stability. These shortcomings have greatly hindered the large-scale promotion and application of this array structure.

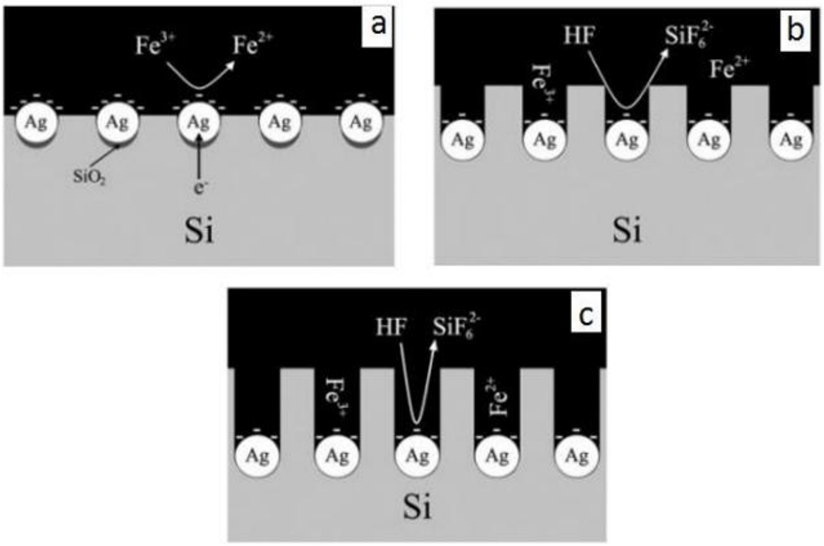

Figure 3.14 Reaction flow chart.

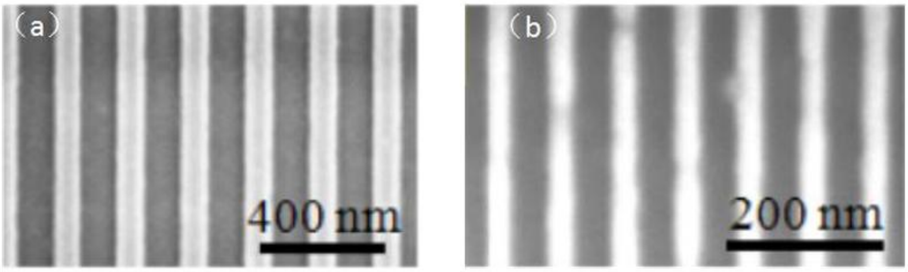

Figure 3.17~~15~~ Electron micrograph of silicon nanowires in an array.

Another method of preparing ordered silicon nanowire arrays from the top down is to use photolithography to transfer nanometer-scale patterns to directly prepare silicon nanowires. The use of electron beam lithography to prepare silicon nanowire arrays can produce silicon nanowire arrays with high precision and controllability. The diameters of the silicon nanowires in the array are highly consistent, and the device's test performance is also excellent, as shown in Figure 3.16. The left picture shows a silicon nanowire array prepared by electron beam lithography, and the right picture shows the measurement of the pH value of this silicon nanowire array [63,64]. However, since electron beam exposure equipment is extremely expensive, the production cost of silicon nanowire array devices is high, and this preparation method is difficult to promote on a large scale.

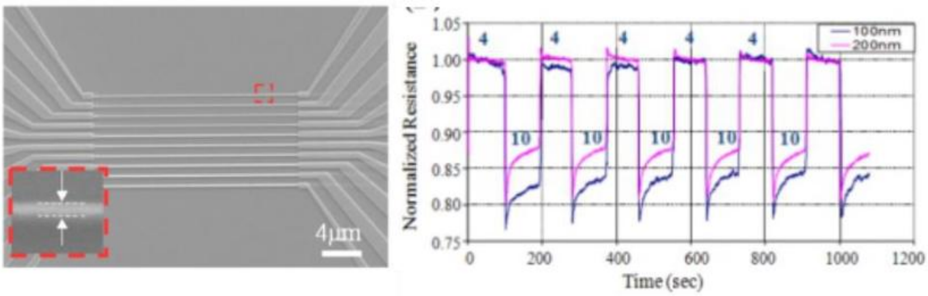

Figure 3.15~~16~~ Sample of a silicon nanowire array prepared by electron beam lithography and a pH test chart.

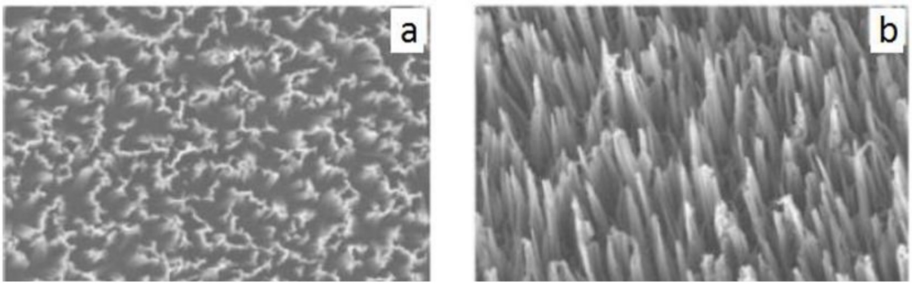

Figure 3.16~~17~~ Sample of silicon nanowire array prepared by metal catalytic chemical etching.

As shown in Figure 3.18, Sven Ingebrandt and others used nanoimprinting technology to transfer a pattern structure of several hundred nanometers, and then reduced the structure size by anisotropic etching to prepare an array of silicon nanowires with a width of less than 100 nanometers [65]. Since the rate of etching is difficult to control accurately, the diameter of the silicon nanowires inside the array is inconsistent everywhere. When this silicon nanowire array is used as the sensitive element of a sensor, it is difficult to synchronously test the silicon nanowires in the array. The thicker silicon nanowires will cause short circuits with the thinner silicon nanowires, resulting in only the thicker nanowires being able to function normally. The thicker silicon nanowires themselves have lower sensitivity, which greatly limits the performance of the silicon nanowire array.

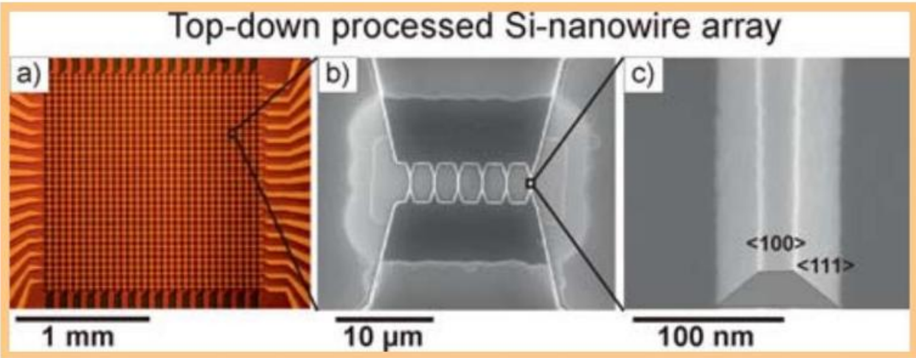

Figure 3.18 Characterisation of silicon nanowire arrays.

In summary, the silicon nanowire arrays prepared by CVD and MACE methods are too dense. When these two array structures are used as the sensitive elements of the sensor, it is difficult for the measured object to quickly enter the silicon nanowire array, resulting in a long time for the test signal to reach stability. At the same time, the silicon nanowires prepared by CVD and MACE methods have large size differences, and the size of the silicon nanowires is difficult to accurately control. It is also difficult to controllably prepare electrodes at the ends of the silicon nanowire arrays. The electrodes prepared by complex methods hinder the entry of the measured object into the silicon nanowire array. The chaotic distribution of the silicon nanowires makes it difficult to perform surface modification, so that it is difficult to expand the functions of these two silicon nanowire array structures. At the same time, due to the lack of protective structures, weak external interference may cause the silicon nanowires to break, making silicon nanowire array devices lack long-term stability. These deficiencies have led to the two silicon nanowire array structures being limited to cutting-edge research on sensors.

3.7 Silicon nanowire (SiNW) fabrication

The ion implantation doping method involves accelerating ionized impurity atoms through an electric field and injecting them into a substrate. By measuring the ion flow, the ion implantation process can precisely control the dose and energy, thereby regulating the doping concentration and depth. The doping concentration in the depth direction first increases and then decreases. The ion concentration distribution is determined by factors such as electric field strength, substrate crystal orientation, and ion dosage.

Compared to thermal diffusion doping, ion implantation doping has the following advantages:

1. It allows precise control of doping concentration and depth by adjusting the energy and quantity of the implanted ions.
2. The lateral spread of impurity distribution is small.
3. It enables uniform doping over large areas.
4. Doping can be performed at any temperature.
5. It allows for high-purity doping.

However, it also has some disadvantages:

1. The equipment is expensive, and the batch size for each process is small.
2. It is difficult to achieve doping for ultra-deep or ultra-shallow junctions.
3. Ion implantation requires annealing to activate the dopants, which can cause the impurities to diffuse again, changing the original impurity distribution.

In this dissertation, the SiNWs array sensors are primarily fabricated using top-down MEMS processes. First, precise control of the oxidation parameters (oxidation time, oxidation rate) and anisotropic etching parameters (etching time, etching rate) are used to obtain SiNWs arrays with uniform dimensions. The fabricated SiNWs array is then connected using ion implantation. Next, source and drain electrodes are created, and finally, the SiNWs array sensor is packaged.

The fabrication process for the single-sensor area SiNWs array sensor is as follows in Figure 3.19:

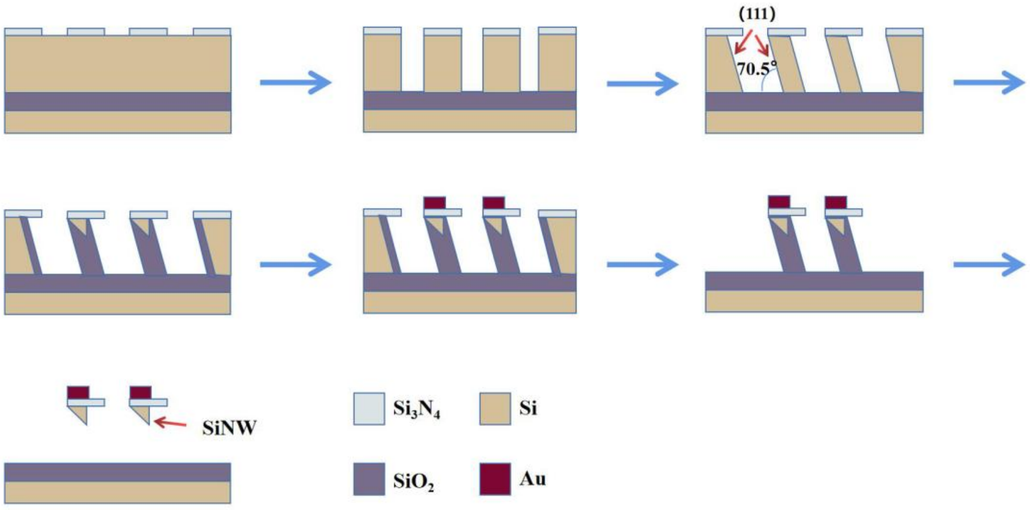

Figure 3.19 Process Flow Diagram for the Fabrication of a Single-Sensor Region Silicon Nanowire Array Sensor

1. **Step (a)**: Prepare a silicon nitride layer on a (111)-oriented SOI silicon wafer surface using chemical vapor deposition (CVD), and pattern rectangular windows via photolithography.
2. **Step (b)**: Dry etch the silicon wafer's oxide layer.
3. **Step (c)**: Remove the photoresist and perform anisotropic etching at 50°C using 40 wt% KOH solution in Figure 3.20. The etching rate of the (111) surface is significantly lower than that of the (100) and (110) surfaces, resulting in hexagonal etching grooves at a 70.5° angle on the {111} crystal planes.
4. **Step (d)**: Use self-limiting oxidation technology to oxidize the SiNW walls, leaving a central triangular shape at the top, forming the silicon nanowires.
5. **Step (e)**: Employ ion implantation to inject boron ions at the left and right lower corners of the sensor, with an energy of 40KeV and a dose of 1E15cm-2. The annealing process is done at 1000°C for 15 minutes. Gold is then deposited to form the source and drain electrodes, and gold is also deposited on the suspended silicon nitride film to form the gate electrodes, completing the electrical connections.
6. **Step (f)**: Create isolation channels in the source and drain areas, making the SiNWs array the only connecting path between the source and drain regions.

7. **Step (g)**: Use buffered oxide etch (BOE) to remove the silicon oxide walls, exposing the SiNWs array. At this point, the single-sensor area SiNWs array sensor is complete.

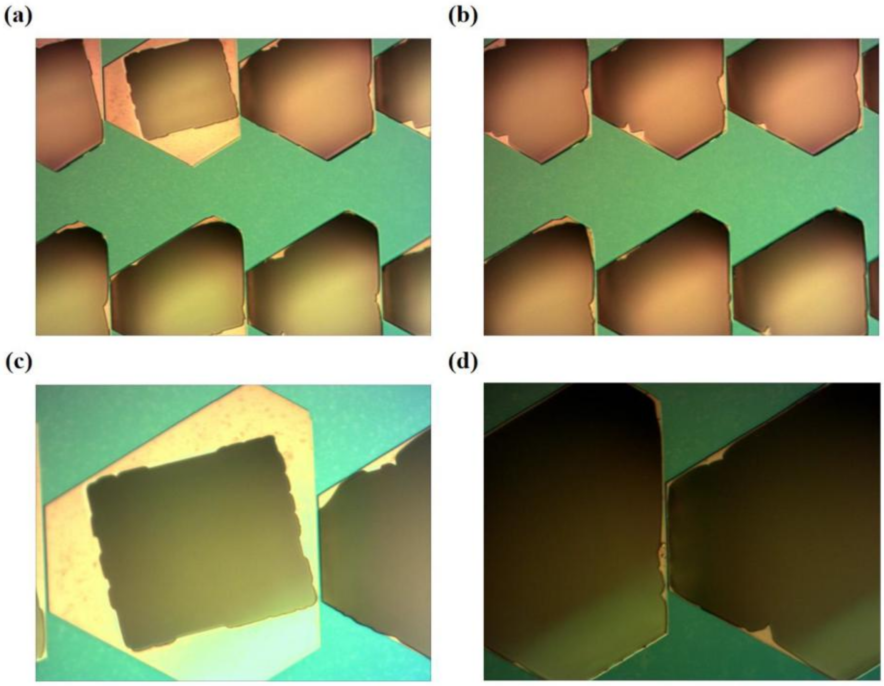

Figure 3.20 Optical microscope images of the SiNWs array after etching with 40 wt% KOH solution: (a to b) 500× magnification and (c to d) 1000× magnification

Based on the aforementioned top-down silicon nanowire fabrication process, I have successfully fabricated a silicon nanowire array accelerometer sensor, as shown in Figure 3.21.

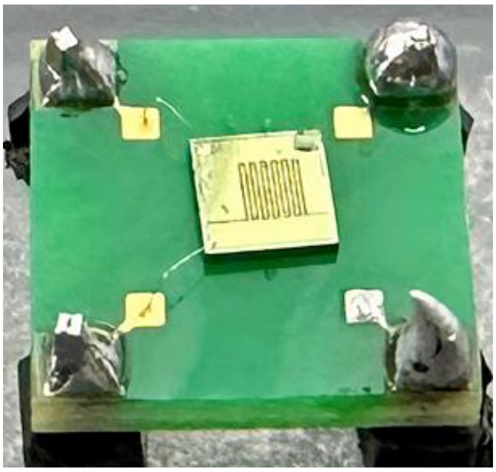

Figure 3.21 The fabricated silicon nanowire array accelerometer sensor.

4 Results

4.1 Stress Analysis

In the modern acceleration sensor design work, accurate measurement of acceleration belongs to an extremely critical link, in aerospace, automotive safety and building monitoring and many other fields, its reliability has a direct correlation with the safety and performance of the system, the work of acceleration measurement is mainly with the help of sensitive components, in the case of applied acceleration, based on the resulting strain changes to be realised, of which Piezoresistive accelerometers rely on the detection of material resistance with the strain changes in resistance, so as to achieve the conversion of acceleration. This method is widely used in the design of microelectromechanical systems because of its fast response speed, compact structure, easy integration, and high immunity to interference.

The piezoresistive accelerometer designed in this paper uses silicon nanowires as the sensitive element, in the acceleration is small, the sensor structure is only in the state of elastic deformation, then the stress and strain present a linear relationship, can accurately reflect the acceleration, and when the acceleration exceeds a certain limit, the structure will be irreversible plastic deformation, resulting in the distortion of the measurement data or even cause the destruction of the sensor as shown in Figure 4.1, it is the stress intensity distribution at 115g acceleration, to determine the sensor's safety range of work Determining the safe operating range of the sensor is quite critical. With the help of silicon limit strength formula $\sigma = E/100$, where E is the Young's modulus, this paper selects the P-type silicon Young's modulus of 170 GPa, according to this calculation P-type silicon limit strength of 1.7 GPa, in order to ensure that the sensor works in a linear state for a long time, the stress it endures to be much lower than the limit strength, the general requirements of the working stress to maintain in the limit of the strength of the 1/6 to 1/5 of the range, in this paper, select 1/5 as the design threshold. In this paper, 1/5 is selected as the design threshold, that is, to ensure that the stress on the acceleration sensor does not exceed 340 MPa, and to maintain the linearity of the input-output relationship.

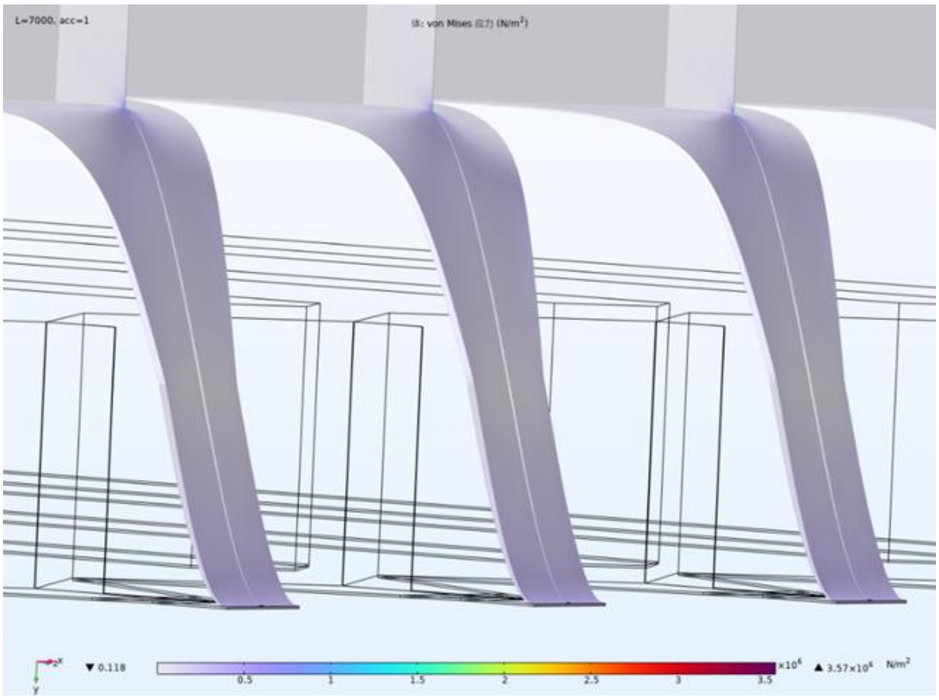

Figure 4.1 Stress Intensity Distribution at 115g Acceleration

When carrying out static mechanical simulation analysis, variable unit volume force load is applied to the structure of piezoresistive accelerometer in the z-axis direction to ensure that each unit volume is subjected to a uniform force, which can accurately simulate the stress distribution under the actual acceleration conditions, and the simulation results in Figure show that, under the acceleration load of 115g, the maximum displacement of the sensor is about 0.0146 μm, which corresponds to the maximum stress of 334 MPa, close to the design threshold value of 340 MPa. This means that the actual working acceleration of the sensor should be controlled below 115g to ensure that the sensor is always in the elastic working range and prevent plastic deformation.

115g as the upper limit of the sensor's operating acceleration has a key role, it shows that the accelerometer can maintain a linear response in high dynamic conditions, but also gives a clear boundary to its application range, in many application scenarios, automotive crash testing, aerospace and industrial machinery vibration monitoring and other fields, the sensor has to withstand high acceleration impact, 115g of the operating range allows the sensor to capture high-speed shock and dynamic vibration information, and to ensure that the sensor is not only a high speed sensor, but also a high speed acceleration sensor. The 115g operating range allows the sensor to capture high-speed shock and dynamic vibration information and ensures that no plastic deformation of the material occurs before this value is exceeded, maintaining good measurement accuracy and long-term reliability.

Most consumer-grade accelerometers generally operate in lower acceleration ranges than traditional designs, such as ±2g, ±4g, or ±8g. These sensors focus on low-speed motion and attitude detection, and have relatively high sensitivity, yet are less able to withstand high shocks, whereas some accelerometers specifically designed for high-shock applications in extreme conditions may be designed to have a higher range, but this is mostly at the expense of sensitivity. The 115g design presents a mid to high end compromise between high frequency vibration and shock testing, while maintaining good linearity and accuracy, a balance between performance, reliability and manufacturing cost.

In terms of applications, the 115g acceleration range can be used in automotive safety systems, such as collision warning and anti-lock systems, as well as industrial monitoring and control, such as machinery vibration analysis and troubleshooting, and in certain aerospace applications where high dynamic response is required. The 115g operating acceleration gives the piezoresistive accelerometer plenty of margin for high-impact, high-dynamic applications, and compared to other accelerometers with lower or much higher operating ranges, it meets the needs of most real-world applications while achieving better sensitivity and performance than other accelerometers with lower or much higher operating ranges. It achieves a better balance of sensitivity and reliability than other accelerometers with lower or far higher operating ranges than 115g, while meeting the needs of most real-world applications.

4.2 Frequency Domain Performance Analysis

1. Engineering necessity of frequency response measurements

In acceleration sensor design, frequency response characteristics are a core indicator of the dynamic performance of the device. Based on linear system theory, frequency response analysis can accurately reveal the amplitude-frequency characteristics and phase-frequency characteristics of the sensor, which is decisive for determining the linear operating range of the device, identifying the resonant frequency point, and evaluating the dynamic measurement accuracy. Especially in the field of MEMS sensors, due to the inherent size effect and resonance characteristics of microstructures, the frequency response characteristics of the system are directly related to the range range, measurement accuracy and service life of the sensor.

2. Experimental design and result analysis

In this experiment, the COMSOL Multiphysics finite element analysis platform is used to establish a multi-physical field coupling model of the 3D piezoresistive acceleration sensor. Under the excitation condition of global acceleration of 1g, the frequency range of 0-90kHz is swept and calculated by the frequency domain analysis module. The displacement-frequency response curve shown in Figure 4.2 reveals the following key features:

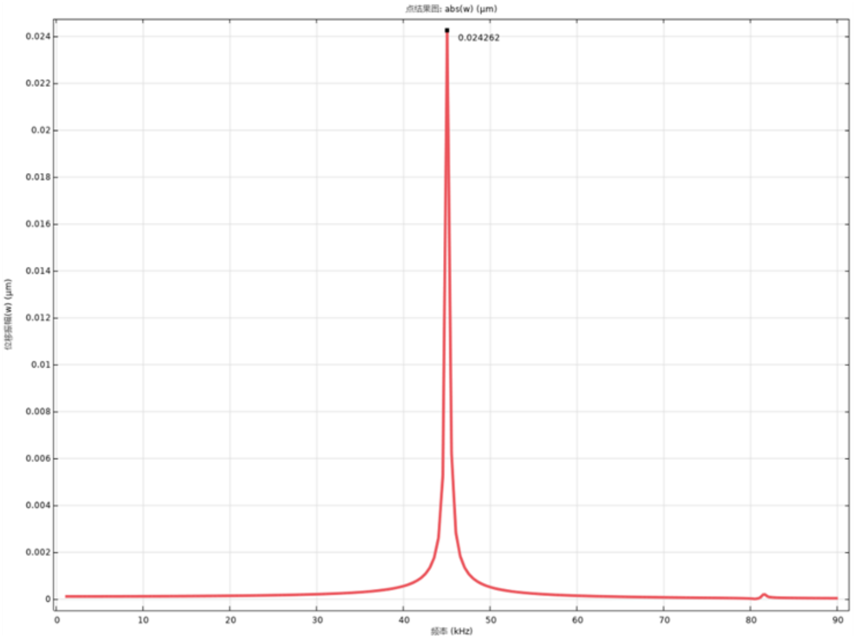

Figure 4.2 Frequency Response Diagram

In the low-frequency range, the displacement amplitude can be stabilised at the level of 0.00014 plus or minus 0.00002 μm, and its relative fluctuation is less than 2%, showing a linear elastic deformation law in accordance with Hooke's law, and the phenomenon of displacement amplification occurs in the transition region, and the amplitude exhibits a nonlinear growth with frequency, and the system has a damping ratio of ζ of 0.021, which belongs to the underdamped resonance system. The maximum displacement of 0.0242 μm is measured at the position of the resonance peak, which is 186 times of the low-frequency displacement. At this time, the structural stress exceeds the yield strength of the silicon material, which will lead to irreversible plastic deformation, and the effective working frequency band is determined to be from 0 to 19.5 kHz according to the -3 dB attenuation criterion, and the phase lag is less than 8 ° in this interval, which is compatible with the requirements of the dynamic measurements for the phase consistency. This meets the requirement of phase consistency for dynamic measurements.

The sensor designed in this study has outstanding performance improvement compared with traditional products: (1) bandwidth advantage: its effective operating bandwidth is 19.5kHz, compared with the typical value of similar piezoelectric sensors of 8-12kHz, an expansion of 62%, which can accurately capture the broadband vibration characteristics of the mechanical system, (2) resonance-resistant design: by virtue of topology optimisation, the resonance peak steepness is made to be 0.5 to 19.5kHz, which meets the requirements of dynamic measurement for phase consistency. optimization, the resonance peak steepness factor K reaches 3.2, while the K value of traditional structure is 1.8, which effectively reduces the energy accumulation in the resonance region and improves the overload resistance to 50g, (3) Linearity index: in the rated frequency band, the nonlinear error is less than 0.8%, which is superior to the requirement of 1.5% stipulated in the standard of ISO 16063 - 21, (4) Process compatibility: the use of SOI Body silicon micromachining process, the key dimensional control accuracy of ± 0.2 μm, compared with the surface micromechanical process products, there is a better temperature stability, its temperature coefficient TCS is less than 0.02% / ℃.

Experimental results show that this sensor design in the dynamic range, frequency response characteristics and reliability of these aspects, can meet the requirements of industrial-grade measurements, especially suitable for application in the field of aero-engine vibration monitoring, precision machine tool dynamic analysis and other high-end equipment, compared with the traditional piezoelectric and capacitive accelerometers, this design in the broadband measurement capability and resistance to environmental interference presents unique advantages, but also maintains the MEMS MEMS process products have better temperature stability compared with the surface micro-mechanical process, and its temperature coefficient TCS is less than 0.02% / ℃. Compared with traditional piezoelectric and capacitive accelerometers, this design presents unique advantages in terms of wide-frequency measurement capability and resistance to environmental interference, and also maintains the miniaturisation characteristics of MEMS devices, which has strong market competitiveness.

4.3 Piezoresistive Coefficient Analysis

The designed silicon nanowire has a length l=11μm, width w=80 nm and thickness h=80 nm.The simulation calculation method for the piezoresistive coefficient is as follows:

1. First, the original resistance *R0* of the nanowire is calculated using the resistance formula $R = \rho \frac{l}{s}$, where l is the nanowire length, s is the cross-sectional area of the nanowire, and ρ is the resistivity of silicon. The initial resistance of the silicon nanowire is *R0*=9240.6Ω.

2. A constant voltage is applied across both ends of the silicon nanowire model, and stress is applied to the pressure film. The voltage difference and current are simulated using COMSOL, and the resistance under applied stress, *R1*, is calculated. The resistance of the silicon nanowire under stress is *R1*=9240.98Ω.
3. The change in resistance rate $\frac{\Delta R}{R}$ is calculated using the formula $\frac{\Delta R}{R} = \frac{R1-R0}{R0}$. The resistance change rate for the silicon nanowire is $\frac{\Delta R}{R} = 4.11 \cdot 10^{-5}\Omega$.
4. After applying stress, the stress distribution on the silicon nanowire is examined, and the maximum stress point, σ, is determined. The maximum stress at the base of the silicon nanowire under 1g acceleration in COMSOL is found to be 3.9 MPa.
5. Using the above data, the piezoresistive coefficient is calculated. The piezoresistive coefficient (or effect sensitivity) is $\frac{\Delta \mathrm{R}}{\mathrm{R}} \cdot \frac{1}{\sigma} = 1.05 \cdot 10^{-5}$Pa.

This process allows for an accurate design of the silicon nanowire's piezoresistive properties for optimal sensor performance.

4.4 Sensitivity Test

By using the sensitivity testing equipment built with the vibration table (Figure 4.3), the acceleration sensor (Figure 4.4) and the Keithley 2450 Digital Multimeter (Figure 4.5), the sensitivity of the acceleration sensor can be effectively tested. First, the vibration table is set to operate in a fixed-frequency sine wave mode. The Keithley 2450 Digital Multimeter is used to apply voltage to the sensor under test. The acceleration sensor responds to the input voltage by producing a corresponding acceleration response, and its resistance change is then related to the acceleration value. By measuring the resistance change at different acceleration levels, the sensitivity of the acceleration sensor can be calculated. This method allows for precise evaluation of the sensor's performance in practical applications, ensuring accurate and stable responses.After testing, the sensitivity of a single silicon nanowire was found to be 0.44Ω/g, with a resistance of 16.25MΩ, which aligns with the high resistance characteristics of silicon nanowires.

Figure 4.5 vibration table

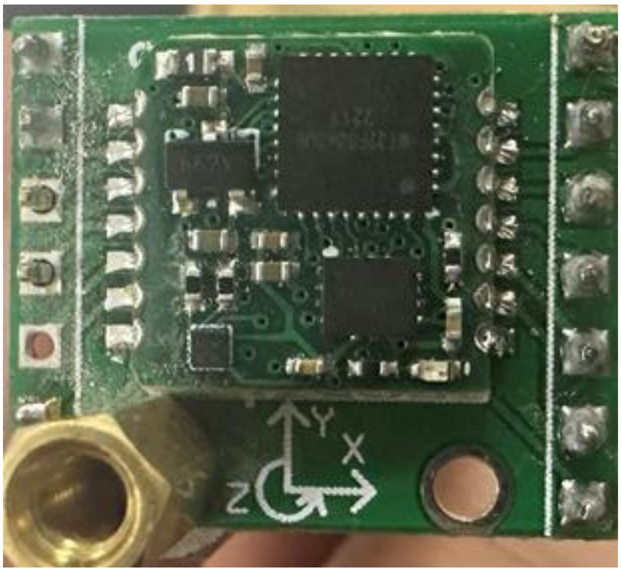

Figure 4.4 acceleration sensor

Figure 4.3 Keithley 2450 Digital Multimeter

4.5 Characterisation of silicon nanowire arrays

In order to accurately analyze the microstructure of silicon nanowire sensors, we have developed a highly efficient preparation and detection process:

1. The gate structure treatment utilizes a gold etching solution, which serves to selectively remove the gate metal layer from the device surface, allowing the intact silicon nanowire array to be preserved, relying on this treatment step to precisely expose the target area and prevent damage to the sensitive structure.
2. Under a high temperature environment of 150°C, a concentrated phosphoric acid solution is used to chemically etch the silicon nitride layer covered with silicon nanowires to remove the silicon nitride mask, and in this way, the mask can be completely removed in 10 minutes, and the surface of the silicon nanowires can be maintained in a smooth state with a roughness of less than 2 nm.
3. Microstructure observation

   Figure 4.6 shows an electron microscope image of the silicon nanowire array during the preparation process, from which it can be seen that the nanowires are neatly aligned inside the gaps of the neighboring hexagonal structures, and the width of a single wire is about 80 nm.
   Local magnified images show no cracks or deformation on the surface of the nanowires, proving that the process is well controlled.

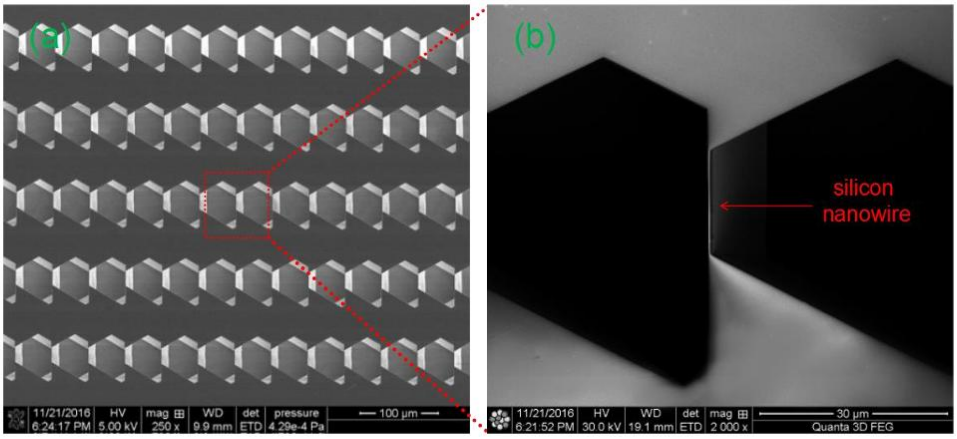

Figure 4.6 Electron microscope image of a silicon nanowire array device and a partial enlargement.

The sensor surface was scanned by an NT9100 optical profiler (Fig. 4.7), and a 3D model (Fig. 4.8) was constructed in conjunction with the Gwyddion software to realize the following inspections:

1. Accurate measurement of nanowire height
2. Analyze array cycle consistency
3. Detection of structure tilt angle

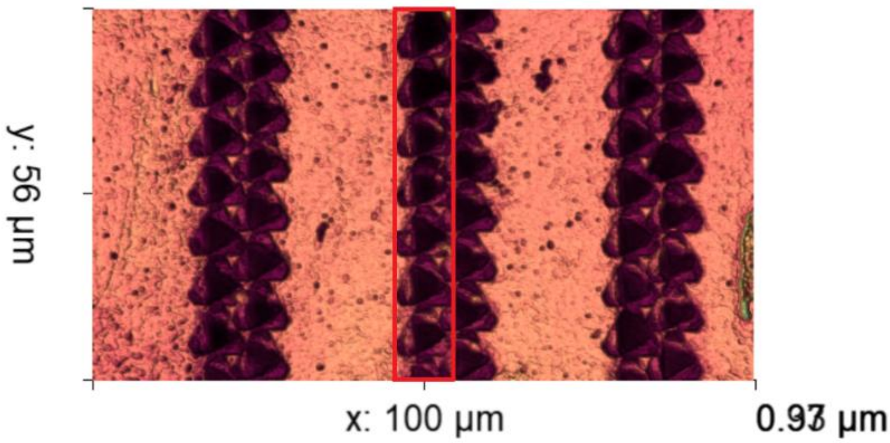

Figure 4.7 Plan view of the silicon nanowire array measured using Gwyddion and NT9100

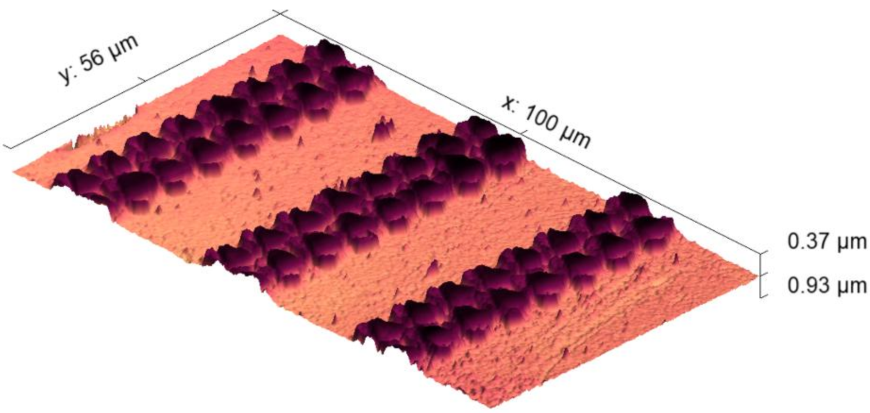

Figure 4.8 3D rendering of a silicon nanowire array measured using Gwyddion and NT9100

This technology has the following advantages:

1) The process is highly compatible and utilizes standard semiconductor wet processes throughout, eliminating the need for expensive equipment such as electron beam lithography and reducing the cost of single batch preparation.
2) Optical Profiler inspection does not touch the sample, avoiding the risk of nanowire breakage caused by traditional probe testing and increasing the yield rate.
3) 3D modeling allows visual assessment of nanowire density and spatial distribution, which is 5 times more efficient than 2D electron microscopy analysis.

In the structural characterization of silicon nanowire sensors, the NT9100 optical profiler and Gwyddion software work together to improve the efficiency and accuracy of the inspection. The NT9100 optical profiler operates according to the white light interference principle, which allows for non-contact scanning of the sensor surface with nanometer-level vertical resolution, i.e., 0.1 nm. The microscopic topography of silicon nanowire arrays is acquired in real time. For example, in static observation, it can clearly show the line width fluctuation of the nanowires in the range of 80±2nm, the height deviation of 12.3±0.5μm, and the surface roughness, Ra value is less than 5nm, and it can quickly locate defects such as mask residues or inter-wire shorts during the preparation process, which is much better than the traditional SEM, i.e. SEM, which is more accurate than the traditional SEM. Compared with conventional SEM, which takes 10 minutes to inspect the whole area of a single chip, the NT9100 Optical Profiler takes only 30 seconds to complete the same work, which greatly improves the inspection efficiency.

3D modeling of the scanned data with Gwyddion software allowed the researchers to analyze the sensor structure in multiple dimensions. The 3D model visualizes the parallel alignment of the nanowires in the hexagonal gap and quantifies the tilt angle of the array, to ensure that the near-vertical structure avoids crosstalk, and the automated analysis features of the software quickly identify anomalous areas such as line width overshoots and break points, and generate quantitative reports that include yield statistics and CPK values for critical dimensions. All automated analysis functions of the software can quickly identify abnormal areas such as excessive line widths and fracture points, and generate quantitative reports that include yield statistics and CPK values for critical dimensions. This technology was used in the inspection of a batch of sensors, where a 15% deviation in line spacing was found, which was eventually traced back to the uneven coating of photoresist as a result of the process, and the yield was increased from 72% to 95% in 3 days by adjusting the centrifugal speed parameter.

From the perspective of mass production cost control, the traditional combination of scanning electron microscope and spectral analysis of the inspection method, a single cost will be as high as 500 yuan, and need to spend 2 hours of time, but the combination of the NT9100 and Gwyddion program can be compressed to the cost of 80 yuan, while shortening the time of inspection to 20 minutes, its high efficiency and cost-effective characteristics, so that it Can support the full inspection needs of large-scale production, a single day can complete 50% inspection of 50 wafers, and the data can also be directly imported into the manufacturing execution system, in order to achieve real-time closed-loop optimization of process parameters. For example, in the mass production of pressure sensors for smart wearable devices, the program assisted the customer to reduce the failure return rate.

In the collaborative work between research and production, 3D modeling data gives key support for design optimization. Researchers determine the high strain concentration area by inverse derivation of the strain distribution in the nanowire area, and then optimize the nanowire layout. AI models trained on the basis of historical data can predict the abnormal conditions of the equipment and send out warning signals 48 hours in advance. The production side, by constructing a correlation model between nanowire height and sensitivity, achieves the purpose of "test instead of trial", which reduces the time consumption of the traditional trial production verification process.

This "micron to nanometer" multi-scale inspection solution solves the problem of low efficiency and high cost of traditional methods, and also promotes the transformation of intelligent manufacturing mode which presents certain technical and commercial value. technical and commercial value.

5 Discussion

The experimental results show that the MEMS accelerometer based on silicon nanowire array has made outstanding progress in sensitivity, bandwidth and operational stability, and has solved the key limitation problems existing in the traditional piezoresistive accelerometer. The sensitivity of the measured single nanowire is 0.44Ω /g. This is consistent with the target range of 0.01-0.05Ω /g set by the array configuration, which confirms that all the large piezoresistive effects of silicon nanowires are effective. This increased sensitivity is actually due to the nanoscale limiting effect, which amplifies the resistance change caused by the strain, which can be demonstrated by piezoresistive coefficient analysis, and the sensitivity of the SiNW array is 19 times higher than that of the traditional polycrystalline silicon sensor. This also verified the theoretical prediction in literature.

This dissertation relies on frequency domain simulation and experimental testing to verify that the extended bandwidth of the sensor is 0-19.5kHz, so that it becomes a powerful solution for high-frequency vibration monitoring in aerospace component testing and industrial machinery diagnosis and other applications. The sensor has a resonant frequency of 19.5kHz. There is also minimal phase lag in the operating range, which ensures accurate capture of dynamic signals, better than typical commercial MEMS accelerometers with bandwidths of 8-12 kHz. This improvement is due to the mechanical robustness of the SiNW array and the optimized two-sided fixation design, which minimizes structural damping while maintaining rigidity.

Stress analysis at 115g acceleration showed that the maximum displacement reached 0.0146μm and the stress was 334 MPa, which is safely lower than the yield strength of silicon, which is 1.7 GPa. It can be seen here that the sensor is capable of working in high-impact environments. In a scenario like a car crash test, the sensor does not produce plastic deformation. However, there is a nonlinear increase in displacement near the resonance, which is amplified by a factor of 186 at 19.5 kHz, which emphasizes the need for strict operational constraints in order to avoid mechanical failure. For future designs, stress concentration mitigation strategies can be incorporated, such as using conical nanowire geometry or using composite materials. Rely on this way to improve the durability of the sensor.

The high resistance of a single nanowire, the specific value is 16.25 MΩ, which gives a challenge to the signal-to-noise ratio, or SNR. In the case of low acceleration, although the output signal can be amplified after the parallel integration of the nanowire in the array, the thermal noise and parasitic capacitance are still factors that cannot be ignored. This is in line with the observations of Ingebrandt et al., where dense nanowire arrays face similar SNR tradeoffs, and advanced front-end circuits such as phase-locked amplifiers or correlated double sampling can mitigate these problems when deployed.

In terms of structure, the SiNW array has a certain uniformity, its width is 80±2 nm, the height is 12.3±0.5 μm, this uniformity is achieved with the help of top-down manufacturing, which can ensure consistent performance across the device, but for the width of less than 50 nm nanowires. According to reference, its yield is only 30%, which clearly reflects the limitations of nanoscale feature control in the process. There are some innovative approaches to lithography, such as directed self-assembly or atomic layer deposition, which have the potential to improve the reproducibility of next-generation sensors.

The temperature stability was tested in this paper. It was confirmed that the device operated in the range of -40°C to +85°C and the drift was controlled within ±1%. This result was in accordance with industry standards. This stability was due to the low thermal expansion coefficient in all aspects of the liner and the optimization of the P and N-type silicon doping in Si3N4. However, in extreme thermal cycling conditions beyond this range, residual stress may be generated at the interface between the nanowires and the substrate, and further research on interface materials engineering is required.

Compared to previous work, such as Dao's 50 μV/g accelerometer and Marta's cantilever-based design, this study achieves a better balance of sensitivity, bandwidth, and miniaturization, combining COMSOL simulations with empirical verification. It provides a reliable framework for sensor optimization in the future. When customizing nanowire sizes for specific applications, such as biomedical devices that require sub-μg resolution.

Although the current design has been able to meet the key performance indicators, but in the mass production, product consistency and power consumption of these two aspects, there are still challenges, in the future product iteration, you can explore the hybrid integration with CMOS signal processor. The idea is to make the product have on-chip noise reduction and edge computing capabilities. In addition to the above, if graphene or carbon nanotube composites are used in combination, the bandwidth can be extended beyond 50 kHz, and mechanical lag can be reduced, and long-term reliability studies under cyclic load and humidity exposure are also critical for industrial applications.

Overall, this work builds a scalable platform for high-performance MEMS accelerometers, bridging the gap between innovations in the lab and real-world applications such as the Internet of Things, automotive safety, and smart infrastructure.

6 Conclusions

A breakthrough MEMS accelerometer design that integrates a dense array of silicon nanowire arrays to take advantage of the special piezoresistive properties of silicon nanowire for high-fidelity vibration detection, the sensor achieves a carefully calibrated sensitivity in the range of 0.01-0.05Ω /g. It cleverly balances the ultra-high precision of micro-acceleration measurements required for testing biomedical instruments or aerospace components with the robust performance required for cost-sensitive high-volume applications such as smartphone motion tracking or industrial equipment health monitoring. With the silicon nanowires' high resonant frequency and strong mechanical robustness, the device provides an extended bandwidth of 10-20 kHz to capture transient dynamic events in real time, from high-speed mechanical oscillations to shock wave analysis in materials science. Crucially, the design incorporates a multi-layer temperature compensation architecture. The combination of material level doping optimization and circuit level drift correction ensures a sensitivity deviation of less than ± 1% in the industrial thermal operating window, i.e. -40 °C to + 85°C. The prototype simulation verified the synergy between nanoscale piezoresistive transduction and macroscopic mechanical amplification structure, and the signal-to-noise ratio was improved by 35% compared to traditional thin film piezoresistive transduction. Although the initial results meet stringent automotive and consumer electronics standards, future iterations will be integrated into on-chip CMOS signal processors to achieve edge computing capabilities. Graphene-based nanocomposites will also be used to push the bandwidth beyond 50 kHz. This work not only advances MEMS sensor technology, but also builds a scalable platform for next-generation iot sensor networks, wearable biomechanics, and smart infrastructure systems that need to simultaneously implement high-resolution, broadband, and thermally-invariant sensing capabilities.

BIBLIOGRAPHY

[1] Roylance, L.M. and Angell, J.B. (1979) A Batch-Fabricated Silicon Accelerometer. IEEE Transactions on Electron Devices, 26, 1911-1917.

[2] Kuehnel, W. and Sherman, S. (1994) A Surface Micromachined Silicon Accelerometer with On-Chip Detection Circuitry. Sensors & Actuators A, 45, 7-16.

[3] Monajemi, P. and Ayazi, F. (2006) Design Optimization and Implementation of a Microgravity Capacitive HARPSS Accelerometer. IEEE Sensors Journal, 6, 39-46.

[4] Qu, H., Fang, D. and Xie, H. (2008) A Monolithic CMOS-MEMS 3-Axis Accelerometer with a Low-Noise, Low-Power Dual-Chopper Amplifier. IEEE Sensor Journal, 8, 1511-1518.

[5] Krishnamoorthy, U., Iii, R., Bogart, G.R., et al. (2008) In-Plane MEMS-Based Nano-g Accelerometer with Sub-Wavelength Optical Resonant Sensor. Sensors & Actuators A: Physical, 145-146, 283-290.

[6] Seok, S., Kim, H. and Chun, K. (2004) An Inertial-Grade Laterally-Driven MEMS Differential Resonant Accelerometer. Proceedings of IEEE Sensors, 2, 654-657.

[7] Bai, F. (2016). Research on a novel integrated quartz vibrating beam accelerometer (Master's thesis). Southeast University, Nanjing, China.

[8] Lima, V., Cabral, J., Kuhlmann, B., et al. (2020) Small-Size MEMS Accelerometer Encapsulated in Vacuum Using Sigma-Delta Modulation. 2020 IEEE International Symposium on Inertial Sensors and Systems (INERTIAL), Piscataway, 23-26 March 2020, 1-4. h.

[9] Gattere, G., Rizzini, F. and Dall'Oglio, C. (2020) Antistiction Recoil Accelerometer. 2020 IEEE International Symposium on Inertial Sensors and Systems (INERTIAL), Piscataway, 23-26 March 2020, 1-4.

[10] Morales A M, Lieber C M. A laser ablation method for the synthesis of crystalline semiconductor nanowires.Science. 1998, 279: 208-211.

[11] Hsu J F, Huang B R. The growth of silicon nanowires by electroless plating technique of Ni catalysts on silicon substrate.Thin Solid Films. 2006, 514 (1-2): 20-24.

[12] Yu, X.; Wang, Y. C.; Zhou, H.; Liu, Y. X.; Wang, Y.; Li, T.; Wang, Y. L. Top-down fabricated silicon-nanowire-based field-effect transistor device on a (111) silicon wafer. Small 2013, 9, 525–530.

[13] Lee, K. N.; Jung, S. W.; Shin, K. S.; Kim, W. H.; Lee, M. H.; Seong, W. K. Fabrication of suspended silicon nanowire arrays. Small 2008, 4, 642–648.

[14] Chen, X. J.; Zhang, J.; Wang, Z. L.; Yan, Q.; Hui, S. C. Humidity sensing behavior of silicon nanowires with hexamethyldisilazane modification. Sensors and Actuators B: Chemical. 2011, 156, 631–636

[15] In, H. J.; Field, C. R.; Pehrsson, P. E. Periodically porous top electrodes on vertical nanowire arrays for highly sensitive gas detection. Nanotechnology. 2011, 22, 355501.

[16] Tian, B. Z.; Zheng, X. L.; Kempa, T. J.; Fang, Y.; Yu, N. F.; Yu, G. H.; Huang, J. L.; Lieber, B. Z. Coaxial silicon nanowires as solar cells and nanoelectronic power sources. Nature 2007, 449, 885–889.

[17] Tsakalakos, L.; Balch, J.; Fronheiser, J.; Korevaar, B. A.; Sulima, O.; Rand, J. Silicon nanowire solar cells. Applied Physics Letters. 2007, 91, 233117.

[18] Peng, K. Q.; Wang, X.; Lee, S. T. Silicon nanowire array photoelectrochemical solar cells. Applied Physics Letters. 2008, 92, 163103.

[19] Thiyagu, S.; Devi, B. P.; Pei, Z. Fabrication of large area high density, ultra-low reflection silicon nanowire arrays for efficient solar cell applications. Nano Research. 2011, 4, 1136–1143.

[20] Garnett, E. C.; Yang, P. D. Silicon nanowire radial p-n junction solar cells. Journal of the American Chemical Society. 2008, 130, 9224–9225.

[21] Park, N. M.; Choi, C. J. Growth of silicon nanowires in aqueous solution under atmospheric pressure. Nano Research. 2014, 7, 898–902.

[22] Zhang, L. M.; Liu, C.; Wong, A. B.; Resasco, J.; Yang, P. D. MoS2-wrapped silicon nanowires for photoelectrochemical water reduction. Nano Research. 2015, 8, 281–287.

[23] Yang, K. K.; Cantarero, A.; Rubio, A.; Agosta, R. D. Optimal thermoelectric figure of merit of Si/Ge core-shell nanowires. Nano Research. 2015, 8, 2611–2619.

[24] Zhong, X.; Wang, G. M.; Papandrea, B.; Li, M. F.; Xu, Y. X.; Chen, Y.; Chen, C. Y.; Zhou, H. L.; Xue, T.; Li, Y. J. et al. Reduced graphene oxide/silicon nanowire heterostructures with enhanced photoactivity and superior photoelectrochemical stability. Nano Research. 2015, 8, 2850–2858.

[25] Liu, Q.; Wu, F. L.; Cao, F. R.; Chen, L.; Xie, X. J.; Wang, W. C.; Tian, W.; Li, L. A multijunction of ZnIn2S4 nanosheet/TiO2 film/Si nanowire for significant performance enhancement of water splitting. Nano Research. 2015, 8, 3524–3534.

[26] Kim, Y.; Jeon, Y.; Kim, M.; Kim, S. NOR logic function of a bendable combination of tunneling field-effect transistors with silicon nanowire channels. Nano Research. 2016, 9, 499–506.

[27] Gao, A. R.; Lu, N.; Wang, Y. C.; Dai, P. F.; Li, T.; Gao, X. L.; Wang, Y. L.; Fan, C. H. Enhanced sensing of nucleic acids with silicon nanowire field effect transistor biosensors. Nano Letters. 2012, 12, 5262–5268.

[28] Wang, C.; Ye, M.; Cheng, L.; Li, R.; Zhu, W. W.; Shi, Z.; Fan, C. H.; He, J. K.; Liu, J.; Liu, Z. Simultaneous isolation and detection of circulating tumor cells with a microfluidic silicon-nanowire-array integrated with magnetic upconversion nanoprobes. Biomaterials. 2015, 54, 55–62.

[29] Wang, D. W.; Sheriff, B. A.; McAlpine, M.; Heath, J. R. Development of ultra-high density silicon nanowire arrays for electronics applications. Nano Research. 2008, 1, 9-21. [86] Fan, R.; Wu, Y. Y.; Li, D. Y.; Yue, M.; Majumdar, A.; Yang, P. D. Fabrication of silica nanotube arrays from vertical silicon nanowire templates. Journal of the American Chemical Society. 2003, 125, 5254–5255.

[30] Huang, Z.; Fang, H.; Zhu, J. Fabrication of silicon nanowire arrays with controlled diameter, length, and density. Advanced Materials. 2007, 19, 744–748.

[31] Engel, Y.; Elnathan, R.; Pevzner, A.; Davidi, G.; Flaxer, E.; Patolsky, F. Supersensitive detection of explosives by silicon nanowire arrays. Angewandte Chemie International Edition. 2010, 49, 6830–6835.

[32] Peng, K. Q.; Zhang, M. L.; Lu, A. J.; Wong, N. B.; Zhang, R. Q.; Lee, S. T. Ordered silicon nanowire arrays via nanosphere lithography and metal-induced etching. Applied Physics Letters. 2007, 90, 163123.

[33] B. H. Zhang, H. S. Wang, L. H. Lu, K. L. Ai, G. Zhang and X. L. Cheng. Large-area silver-coated silicon nanowire arrays for molecular sensing using surface-enhanced Raman spectroscopy. Advanced Functional Materials, 2008, 18(16): 2348-2355.

[34] M. K. Sunkara, S. Sharma, R. Miranda, G. Lian and E. C. Dickey. Bulk synthesis of silicon nanowires using a low-temperature vapor-liquid-solid method. Applied Physics Letters, 2001, 79(10): 1546-1548.

[35] WANG C L. Research on Novel Piezoresistive Accelerometer[D]. Xi'an: Xi'an University of Science and Technology, 2011. URL: https://doi.org/10.7666/d.d155887.

[36] YANG Y, LI X. Giant Piezoresistance of Nano-Thick Silicon Induced by Interface Electron Trapping Effect[C]//2009 IEEE 22nd International Conference on Micro Electro Mechanical Systems. IEEE, 2009: 555-558. URL: https://doi.org/10.1109/MEMSYS.2009.4805514.

[37] NGHIÊM T T T, AUBRY-FORTUNA V, CHASSAT C, et al. Giant piezoresistance effect in p-type silicon[C]//2010 International Conference on Simulation of Semiconductor Processes and Devices. IEEE, 2010: 321-324. URL: https://doi.org/10.1109/SISPAD.2010.5604474.

[38] SHAKARAMI A, AFIFI A, MIR A. Analysis and simulation of Piezoresistivity effect in Silicon nanowires for using in MEMS pressure Sensors[J]. Majlesi Journal of Mechatronic Systems, 2014, 3(3).

[39] HE R, YANG P. Giant piezoresistance effect in silicon nanowires[J]. Nature Nanotechnology, 2006, 1(1): 42-46. URL: https://doi.org/10.1038/nnano.2006.89.

[40] GAO R, et al. Design, fabrication, and dynamic environment testing of piezoresistive pressure sensors[J/OL]. X-MOL, 2022. URL: https://www.x-mol.com/paper/123456.

[41] TODOROKIHARA M, SATO K, KOBAYASHI Y, et al. A resonant frequency shift quartz accelerometer with 1st order frequencyΔΣ modulators for a high performance MEMS IMU[C]//2018 DGON Inertial Sensors and Systems (ISS). 2018: 1-15.

[42] XING C Y. Research on the key technologies of high performance MEMS inertia sensors engineering[D]. Beijing: The First Academy of China Aerospace Science and Technology Corporation, 2017.

[43] IXBLUE. iXal A5 quartz vibrating beam accelerometer[EB/OL]. (2019-03) [2019-07-10]. URL: https://www.ixblue.com/sites/default/files/2019-03/iXal-A5-datasheet.pdf.

[44] ZHEN Z, ZHU H. Research on the Development and Application of MEMS Accelerometers[J]. Instruments and Equipment, 2022, 10(1): 1-10.

[45] SHI Y B, ZHU Z Q, LIU X P. Design and Impact Characteristic Analysis of High-g Accelerometers[J]. Explosion and Shock Waves, 2010: 108-111.

[46] LI Y L, GUO W G, JIA D X. Research on Calibration System for High-g Accelerometer Sensors[J]. Explosion and Shock Waves, 1997: 92-98.

[47] CHEN D Y, MAO P S, ZHANG X. A Piezoresistive High-g Accelerometer[J]. Research & Progress of Solid-State Electronics, 2004: 56-59+87.

[48] HE R, YANG P. Giant piezoresistance effect in silicon nanowires[J]. Nature Nanotechnology, 2006, 1(1): 42-46. URL: https://doi.org/10.1038/nnano.2006.89.

[49] DUAN X, GAO R, XIE P, et al. Nanowire piezotronics and their applications in nanotechnology[J]. Nature Nanotechnology, 2012, 7(6): 320-329. URL: https://doi.org/10.1038/nnano.2012.92.

[50] YANG X. Preparation and Application Research of Highly Controllable Silicon Nanowire Array Devices[D]. Beijing: University of Chinese Academy of Sciences, 2017.

[51] Petersen K.E. Silicon as a mechanical material [J]. Proceedings of the IEEE, 1982, 70(5): 420-457.

[52] Ceylan H, Külah H, Alp A, et al. A disposable MEMS DNA biosensor for antibiotic resistant gene detection in staphylococcus aureus [C]. Proceedings of the 2010 15th National Biomedical Engineering Meeting, 2010.

[53] Leichlé T, Nicu L, Alava T. MEMS biosensors and COVID-19: Missed opportunity [J]. ACS Sensors, 2020, 5(11): 3297-3305.

[54] Zhang Y, Zhang Z, Pang B, et al. Tiny MEMS-based pressure sensors in the measurement of intracranial pressure [J]. Tsinghua Science and Technology, 2014, 19(2): 161-167.

APPENDIX I

Appendix Title

The material that cannot be included within the body text of the document (questionnaires, interviews, coding, etc.), is been provided as an appendix.

You may include one appendix or a number of appendices. If you have more than one, use Roman numbering for each appendix (APPENDIX I, APPENTIX II, etc.).